Coastal REsearch And Transportation Education
Tier 1 University Transportation Center
U.S. Department of Transportation

Quantifying Vessel Propeller Wash Impacts on Sedimentation in Shallow-Bay Ports and Waterways

January 29, 2026

(1) Jens Figlus, Ph.D., Associate Professor at Texas A&M University, Department of Ocean Engineering, 200 Seawolf Parkway, Galveston, TX 77554; ORCID https://orcid.org/0000-0001-7355-8943; Email: figlusj@tamu.edu
(2) Aaron Lawrence, Graduate Research Assistant at Texas A&M University, Department of Ocean Engineering, 200 Seawolf Parkway, Galveston, TX 77554; Email: lawrenceaggie0211@tamu.edu
(3) Andrew Gombac, Graduate Research Assistant at Texas State University, Ingram School of Engineering, 601 University Drive, San Marcos, TX 78666; Email: adg160@txstate.edu
(4) Stacey Kulesza, Ph.D., P.E., Associate Professor at Texas State University, Ingram School of Engineering, 601 University Drive, San Marcos, TX 78666; https://orcid.org/0000-0003-3283-6235; Email: sekulesza@txstate.edu

Final Research Report
Prepared for:
Coastal REsearch And Transportation Education

Technical Report Documentation Form

1. Report No. 2301-8	2. Government Accession No. 01895206	3. Recipient's Catalog No. n/a

4. Title and Subtitle

Quantifying Vessel Propeller Wash Impacts on Sedimentation in Shallow-Bay Ports and Waterways

5. Report Date

03/23/2026

6. Performing Organization Code

n/a

7. Author(s)

Jens Figulus, Ph.D Assoc. Prof. Texas A&M Dept Ocean Engineering
Aaron Lawrence, Grad RA at Texas A&M Dept Ocean Engineering
Andrew Gombac, Gad RA at Texas State University Ingram School of Engineering
Stacey Kulesza, Ph.D. Assoc. Prof at Texas State University Ingram School of Engineering

8. Performing Organization Report No.

n/a

9. Performing Organization Name and Address

COLLABORATIVE: Texas A&M University 200 Seawolf Paarkway, Galveston, TX
77554 and
Texas State University, 601 University Drive, San Marsos, TX 78666

10. Work Unit No. (TRAIS)

n/a

11. Contract or Grant No.

69A3552348330

12. Sponsoring Agency Name and Address

Office of the Assistant Secretary for Research and Technology
University Transportation Centers Program
Department of Transportation
Washington, DC United States 20590

13. Type of Report and Period Covered

Final Project Report
January 29, 2026

14. Sponsoring Agency Code

OST-R

15. Supplementary Notes

https://create.engineering.txst.edu/

16. Abstract

Shallow-bay ports and waterways in bay systems along the Gulf Coast of America are critical transportation infrastructure and the Nation’s economic drivers. Vessel propeller wash is the water movement induced by the forces generated from propeller rotation as vessels transit shipping channels. It has the potential to suspend sediment that can then be transported throughout the system, leading to potential sedimentation issues. In this study, field measurements using a vessel-mounted Acoustic Doppler Current Profiler (ADCP) and echo sounder system were conducted in the Houston Ship Channel (HSC) in Galveston Bay, Texas, by traversing the HSC back and forth with a survey vessel immediately after passage of a large ship. The obtained high-resolution 3D velocity and acoustic amplitude return values were processed to quantify suspended sediment concentration (SSC) and suspended sediment flux throughout the water column for around 80 different vessels transiting the HSC. Results indicate that vessel-induced SSC in the ship channel and along the slopes can reach values around 1 g/L, two orders of magnitude larger than background concentrations. Furthermore, suspended sediment fluxes close to 200 g/s perpendicular to the channel axis have been estimated from the field measurements. Simultaneous electrical resistivity measurements via an instrumented tow cable were used to test another measuring technique to assess suspended sediment concentration in the water column caused by large vessels. Although the signals were too small to image the SSC, the average electrical resistivity within the HSC was significantly different when vessels were and were not present in the same locations. Similarly, the electrical resistivity was not significantly different when two transects with vessels were compared or two transects without. Thus, the electrical resistivity data provide further evidence that the vessels induce SSC in the ship channel. The quantifications of SSC and flux and statistical significance of electrical resistivity differences highlight the importance of propeller wash contributions to persistent shoaling issues in the HSC and provide an opportunity to further develop prediction tools for sediment movement and management guidelines on how to mitigate siltation in our Nation’s waterways.

17. Key Words Ship Channel Shoaling, Field Measurements, Acoustic Doppler Current Profiler, Resistivity Probe, Galveston Bay Texas, Houston Ship Channel, Suspended Sediment Concentration	18. Distribution Statement No Restrictions

19. Security Classification (of this report) Unclassified	20. Security Classification (of this page) Unclassified	21. No. of Pages 68	22. Price n/a

ACKNOWLEDGMENT

This study was funded, partially or entirely, by the U.S. Department of Transportation through the Coastal REsearch and Transportation Education University Transportation Center under Grant Award Number 69A3552348330. The work was conducted at Texas A&M University and Texas State University. The authors thank Dr. Anand Puppala (Texas A&M University), Lori Brownell (Port of Houston), and Ray Newby (Texas Department of Transportation) for their support as project advisory board members. A special thanks also goes out to Eddie Majzlik and his company Echo Ocean Science LLC for assistance with field data collection.

DISCLAIMER

ABSTRACT

Shallow-bay ports and waterways in bay systems along the Gulf Coast of America are critical transportation infrastructure and the Nation's economic drivers. Vessel propeller wash is the water movement induced by the forces generated from propeller rotation as vessels transit shipping channels. It has the potential to suspend sediment that can then be transported throughout the system, leading to potential sedimentation issues. In this study, field measurements using a vessel-mounted Acoustic Doppler Current Profiler (ADCP) and echo sounder system were conducted in the Houston Ship Channel (HSC) in Galveston Bay, Texas, by traversing the HSC back and forth with a survey vessel immediately after passage of a large ship. The obtained high-resolution 3D velocity and acoustic amplitude return values were processed to quantify suspended sediment concentration (SSC) and suspended sediment flux throughout the water column for around 80 different vessels transiting the HSC. Results indicate that vessel-induced SSC in the ship channel and along the slopes can reach values around 1 g/L, two orders of magnitude larger than background concentrations. Furthermore, suspended sediment fluxes close to 200 g/s perpendicular to the channel axis have been estimated from the field measurements. Simultaneous electrical resistivity measurements via an instrumented tow cable were used to test another measuring technique to assess suspended sediment concentration in the water column caused by large vessels. Although the signals were too small to image the SSC, the average electrical resistivity within the HSC was significantly different when vessels were and were not present in the same locations. Similarly, the electrical resistivity was not significantly different when two transects with vessels were compared or two transects without. Thus, the electrical resistivity data provide further evidence that the vessels induce SSC in the ship channel. The quantifications of SSC and flux and statistical significance of electrical resistivity differences highlight the importance of propeller wash contributions to persistent shoaling issues in the HSC and provide an opportunity to further develop prediction tools for sediment movement and management guidelines on how to mitigate siltation in our Nation's waterways.

Keywords: Ship Channel Shoaling, Field Measurements, Acoustic Doppler Current Profiler, Resistivity Probe, Galveston Bay Texas, Houston Ship Channel, Suspended Sediment Concentration

Table of Contents

List of Figures

List of Tables

INTRODUCTION

Motivation

The Houston Ship Channel (HSC) in Galveston Bay, Texas undergoes continuous maintenance dredging throughout the year to maintain safe travel for the 50 to 60 deep-draft vessels and approximately 400 tugboats that traverse it daily (USACE Engineer Research and Development Center, 2025). With this, the ongoing 1-billion-dollar channel expansion Project 11 works to expand the HSC allowing larger vessels to access the port and move more efficiently (Leon, 2023). However, as described by Reed et al. (2008), channels that have undergone expansions in their geometry have experienced increased rates of shoaling. With the increase in vessel traffic with larger and faster moving vessels, it is becoming increasingly important to understand the impacts vessels have on sedimentation. This report discusses findings on vessel propeller wash dynamics and resulting suspended sediments using field data collected in the HSC. Propeller wash induced water velocities and resulting suspended sediment concentration (SSC) are quantified through measurements collected using a vessel-mounted Acoustic Doppler Current Profiler (ADCP) and Echosounder system. Measurements captured the effects of different vessel types, such as containerships, bulk carriers, tankers, and tugboats with various barge configurations as they traversed the HSC. Marine electrical resistivity measurements provide additional evidence of SSC persistence in the HSC.

Background

Large deep draft vessels traversing navigational waterways induce hydrodynamic forces on the surrounding bathymetry. These include currents, waves, and turbulence produced by the geometry of the vessel pushing through the water. In addition, the mechanical propulsion of the vessel through one or more propeller(s) creates a high velocity jet known as propeller wash. Propeller wash velocities can create large shear forces on the bed, suspend sediments, and distribute them throughout the water column. These sediments are then available to cause siltation of the channel at lower energy locations that may require increased dredging activities to maintain navigability.

Through experimentation, empirical equations to estimate the propeller wash horizontal velocity profile have been established. A commonly used model separates the flow into three zones as shown in Figure 1. The zones are based on horizontal distance past the propeller nondimensionalized by the propeller diameter. For a 1-m-diameter propeller, for example, the efflux zone ranges from zero to 0.35 m, whereas the zone of flow establishment is located between 0.35 and 3.25 m. Past the 3.25-m-mark away from the propeller lies the zone of established flow. All measurements collected and analyzed in this report are located well into the established flow zone. The velocity profile and its evolution over the distance away from the rotating propeller is dependent on the dimensions of the propeller and the thrust it is generating.

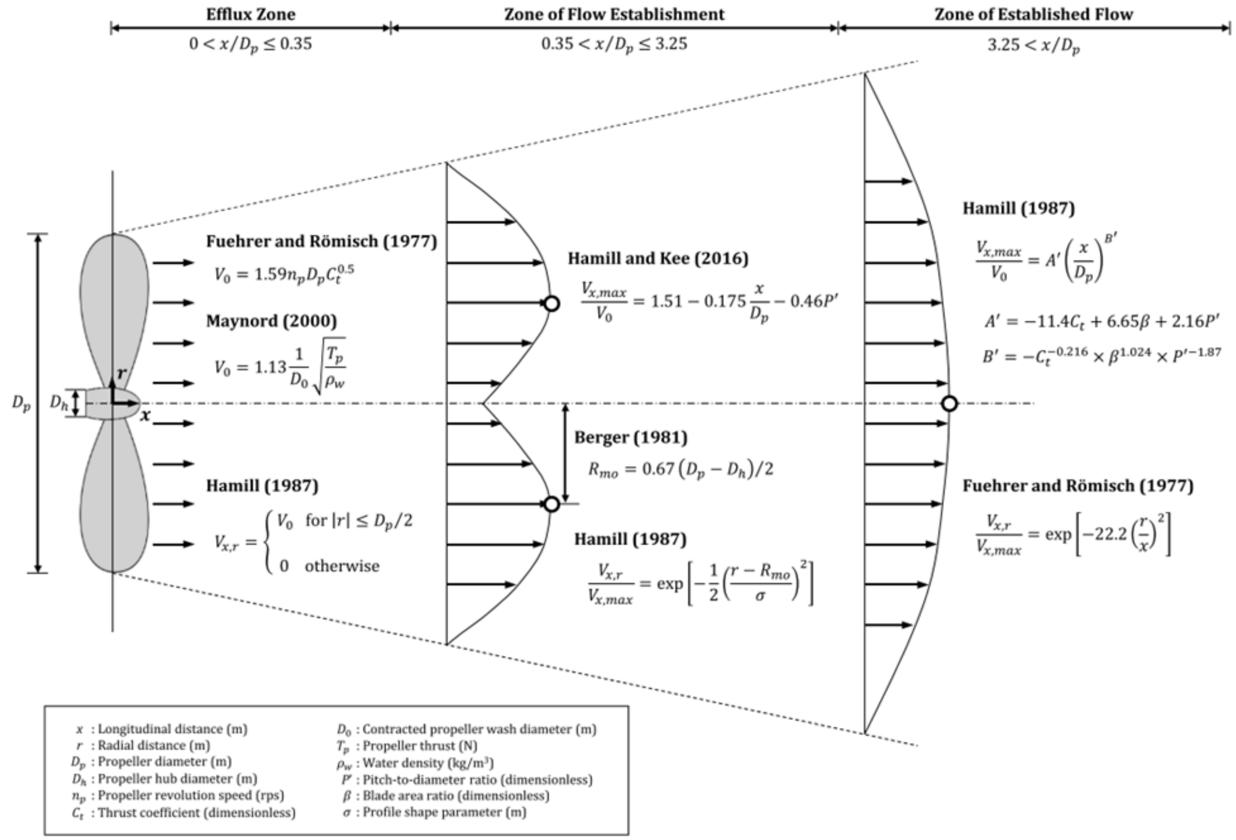

Figure 1. Two-dimensional schematic and empirical velocity equations for various hydrodynamic zones of flow behind a rotating propeller from Craig et al. (2023).

Hong et al. (2016) constructed an experimental apparatus to compare results to the semi-empirical equations established by Hamill (1987) shown in Figure 1. The apparatus consisted of a flat bed, a bubble generator, a propeller, and an Acoustic Doppler Velocity Profiler (ADVP). The measured velocities were plotted against predictions from Hamill (1987) in Figure 2 which shows that the formula can approximate the magnitude and geometry of the velocity profile relatively well. These velocities however do not consider the effects of a moving vessel's own pressure and velocity field on the hydrodynamics and turbulence of the propeller jet (Craig et al., 2023).

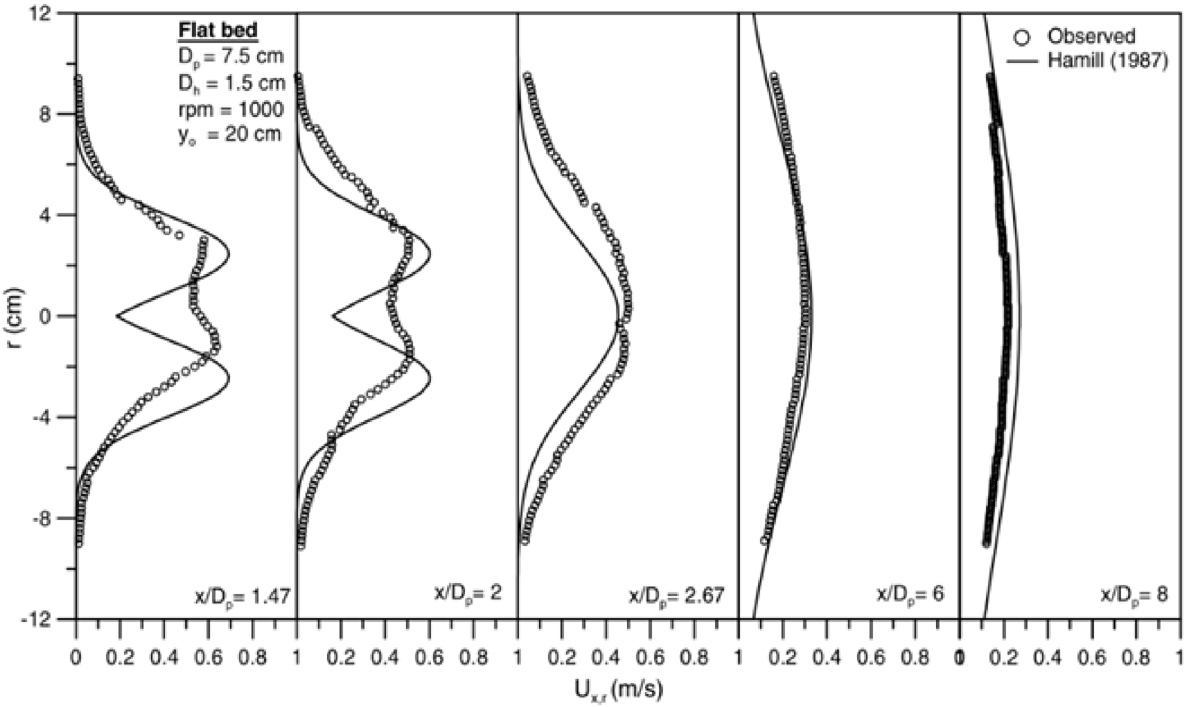

Figure 2. Comparison of physical and numerical model results for two-dimensional velocity profile behind a rotating propeller from Hong et al. (2016).

Analytical predictions of the high velocity jet generated by a rotating propeller can be used to estimate sediment suspension. This is done by using the velocity profile and magnitude to determine the bed shear stress (Craig et al., 2023). However, current sediment models do not include this highly turbulent flow and instead estimate sediment suspension by the pressure wave and wake induced by the vessel geometry moving through the water (e.g., Reed et al., 2008). In addition, vessel propeller wash effects are typically not included. An understanding of suspended sediment quantities induced by vessel propeller wash is important in assessing channel shoaling potential and maintenance dredging requirements, especially as vessel size and transit numbers increase. The use of a vessel-mounted ADCP on a survey boat traversing the ship channel back and forth after passage of a deep draft vessel to quantify SSC allows for relatively accurate capture of the sediment plume and its immediate evolution.

Acoustic profilers utilize the backscattered sound from particles within the fluid being measured to collect various types of data, while the amplitude of the backscattered sound wave is typically used as a gauge for the accuracy of the measurement (Landers et al., 2016). An instrument recording the backscattered amplitude can be calibrated to determine SSC through water samples taken at various points. Similar work performed by Gadgil (2021) determined average quantities of sediment concentrations behind passing vessels using echosounder data as shown in Figure 3. In that dissertation, a background reference concentration was determined using bed and particle characteristics related to a background decibel measurement. These values were then combined with liquification concentrations to estimate total impacts of the passing vessel (Gadgil, 2021).

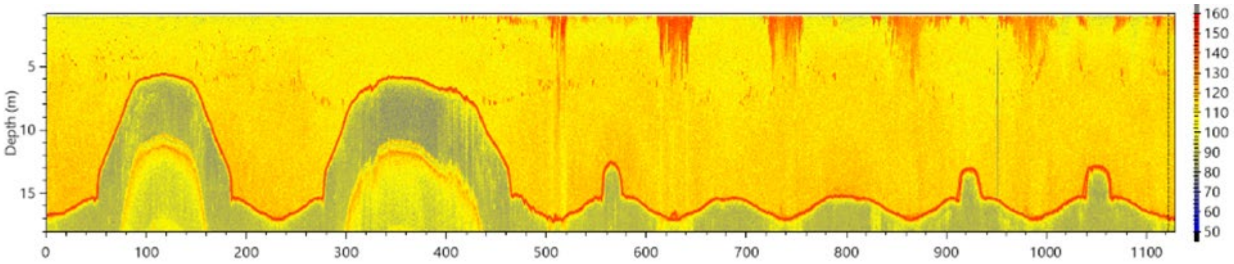

Figure 3. Raw vessel-mounted echosounder data from Corpus Christi Bay, Texas (Figlus and Song, 2020), analyzed for suspended sediment concentration by Gadgil (2021).

However, attenuation of the sound wave traveling through the water column was not taken into consideration and may be the reason for the relatively high concentrations estimated at the surface and not towards the bottom as shown in laboratory experiments in Hong et al. (2016). For acoustic measurements there are three sources of attenuation that may need to be considered: (i) the spreading of the sound wave as it travels, (ii) the energy lost to the medium it is traveling through, and (iii) energy lost as it passes through particles. Once attenuation has been corrected for in the measured acoustic backscatter then it can be related to a known sediment concentration to calibrate the instrument and relate the corrected backscatter amplitude to SSC through (1),

$$C = \log(SSC) - 0.1CB \quad (1)$$

where C is the calibration coefficient, and CB is the corrected backscatter in dB. For aquatic acoustic measurements, the corrected backscatter is typically represented by a water corrected backscatter (WCB) or a sediment corrected backscatter (SCB)

Electrical resistivity is a material's ability to resist the flow of electrical current per unit distance. A four-electrode electrical resistivity measurement injects current directly into a pair of electrodes (current electrodes) and then a resulting potential difference is measured across a second pair of electrodes (potential electrodes) (Everett, 2013). Through a series of these measurements, a resistivity profile of the subsurface can be developed. Electrical resistivity tomography is a traditionally land based geophysical measurement which has applications in site characterization, void detection, groundwater monitoring, and groundwater-surface water interactions (FHWA, 2019; Konaté et al., 2023; Pearson et al., 2022; Koehn et al. 2019). In these land-based surveys, electrodes are connected through a cable and coupled to the ground with stainless steel stakes (Binley, 2015); however, it is possible to conduct electrical resistivity surveys in marine environments, either through a submerged stationary cable or towed electrode cable, known as marine electrical resistivity tomography. Stationary marine surveys can image scour infill material and detect saltwater intrusion (Gombac et al., 2025; Swarzenski et al., 2007). Towed marine electrical resistivity surveys can determine rock strata beneath the water and detect shipwrecks in shallow waters (Rucker and Noonan, 2023; Passaro, 2010). Note, the applications of marine electrical resistivity in the above cases look at the soils beneath the water whereas Amidu and Dunbar (2008) discuss the use of a towed marine electrical resistivity survey to image the salinity within the water column for a reservoir in Waco, Texas. The use of marine electrical resistivity in this study is similar, looking at changes in electrical resistivity of the water column due to the suspension of sediments in the HSC.

METHODS

Field Data Collection

Three separate data collection field campaigns conducted on January 30th, 2024 (Campaign 1, C1), August 8th, 2024 (Campaign 2, C2), and May 14th, 2025 (Campaign 3, C3) utilized a vessel-mounted Nortek Signature 1000 ADCP, as seen in Figure 4. All field campaigns took place in the HSC near Eagle Point in San Leon, Texas (Figure 5). The ADCP was mounted to the port side of the survey vessel 1.2 m below the waterline by a vertical pole with a GNSS antenna on top so that it was directly above the instrument. Equipment checks were performed at the boat dock, after which the Signature 1000 ADCP was removed from the water during transit by rotating the apparatus around its mount. The survey vessel then traveled to the HSC where the instrument and towed electrical resistivity cable were redeployed so that data collection could begin. The segment of the HSC where measurements were conducted is located between Buoy 55 and 65 (Figure 5). Outbound vessel direction (i.e., from the Houston Ports to the Gulf) is from Buoy 65 to Buoy 55.

Figure 4. Photos of Signature 1000 ADCP inside teardrop enclosure (left) and GNSS antenna on top of side-mounted instrument pole (right).

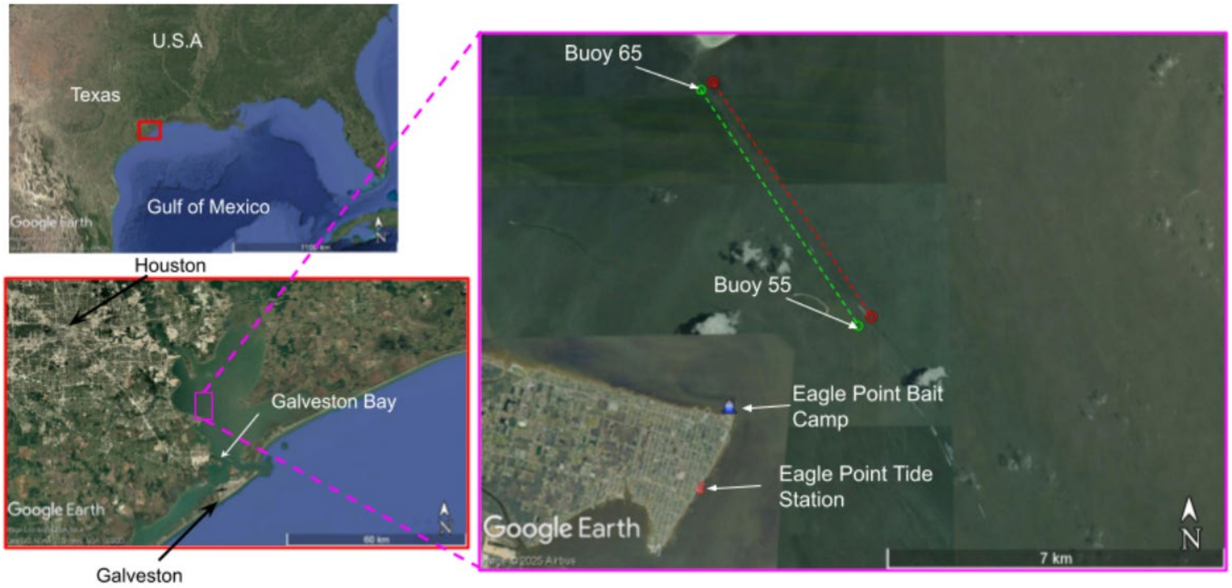

Figure 5. Field site location map (Google Earth, 2025).

Environmental Conditions

The weather on January 30th, 2024, had no precipitation and wind speeds did not exceed 5.9 m/s. The tidal range was approximately 12 cm with high tide peaking at 8 cm and low tide peaking at -4 cm in reference to the Mean Lower Low Water (MLLW) datum. Figure 6 and Figure 7 show snapshots of the relevant wind and water level data during C1 provided by National Oceanic and Atmospheric Administration (NOAA) Station 8771013 (Eagle Point, Galveston Bay, TX).

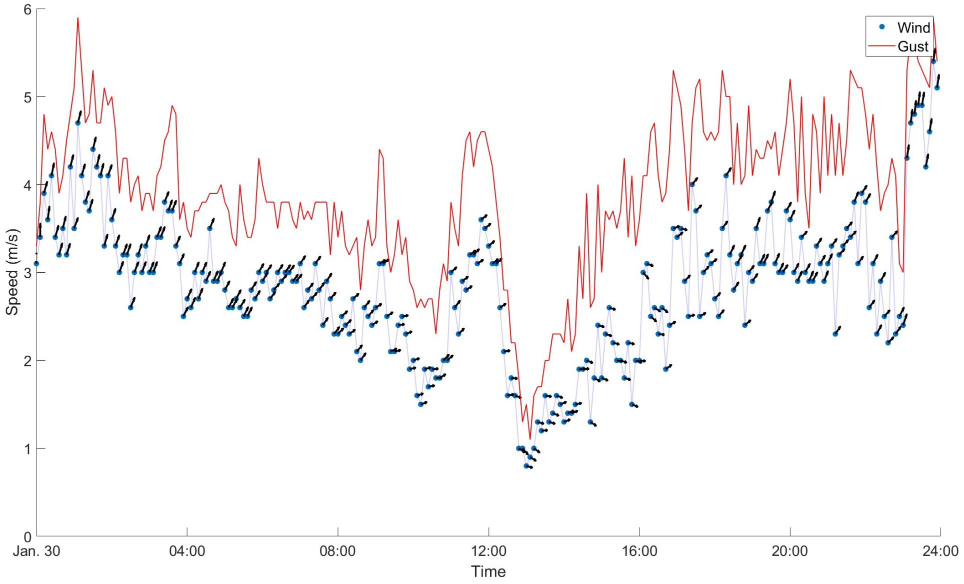

Figure 6. Wind speed and direction measured at NOAA Station 8771013 on January 30th, 2024 (C1).

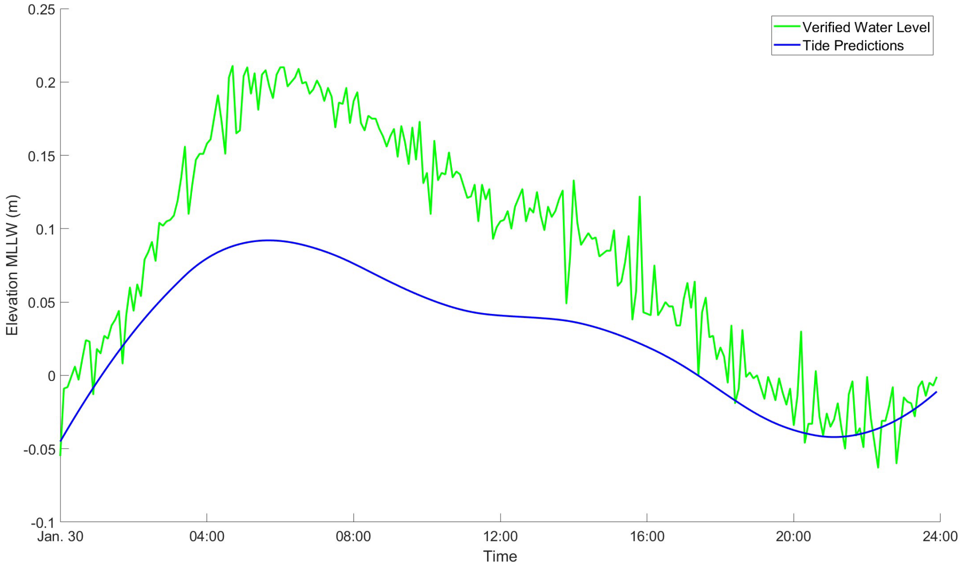

Figure 7. Predicted tide and Verified water levels measured at NOAA Station 8771013 for January 30th, 2024 (C1).

On August 8th, 2024, during C2, there was no precipitation, and wind speeds did not exceed 5.8 m/s. The tidal range was approximately 15 cm with high tide peaking at 26 cm and low tide peaking at 11 cm in reference to the Mean Lower Low Water (MLLW) datum. Figure 8 and Figure 9 show snapshots of the relevant wind and water level data during C2 provided by NOAA Station 8771013 (Eagle Point, Galveston Bay, TX). These conditions allowed for minimal sediment transport resulting from wind and tidal currents, which would add to background concentrations and flux. No wave data are available for the Eagle Point station. However, the influence of wind waves on the survey vessel was relatively minor due to the low wind speeds and can be neglected in comparison to passing vessels' primary and secondary waves.

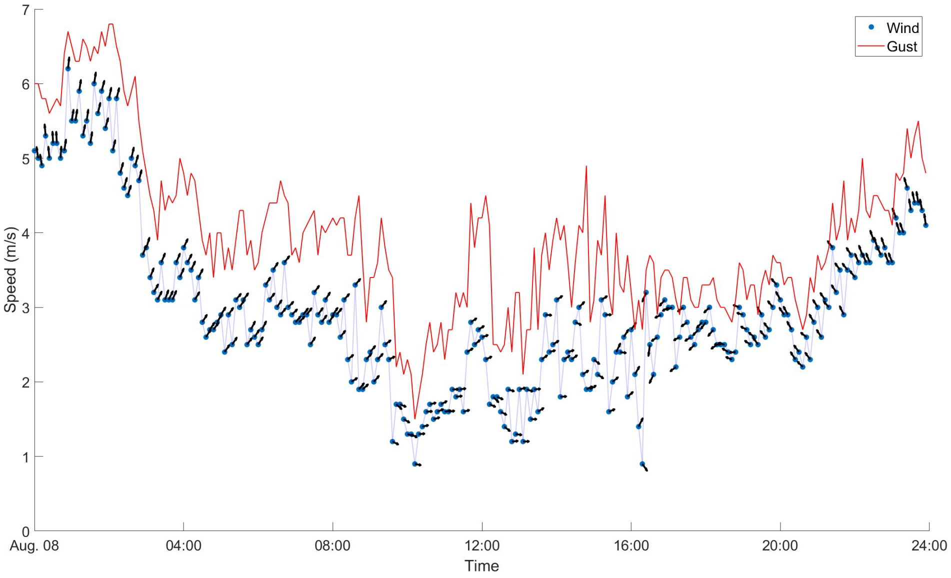

Figure 8. Wind speed and direction measured at NOAA Station 8771013 on August 8th, 2024 (C2).

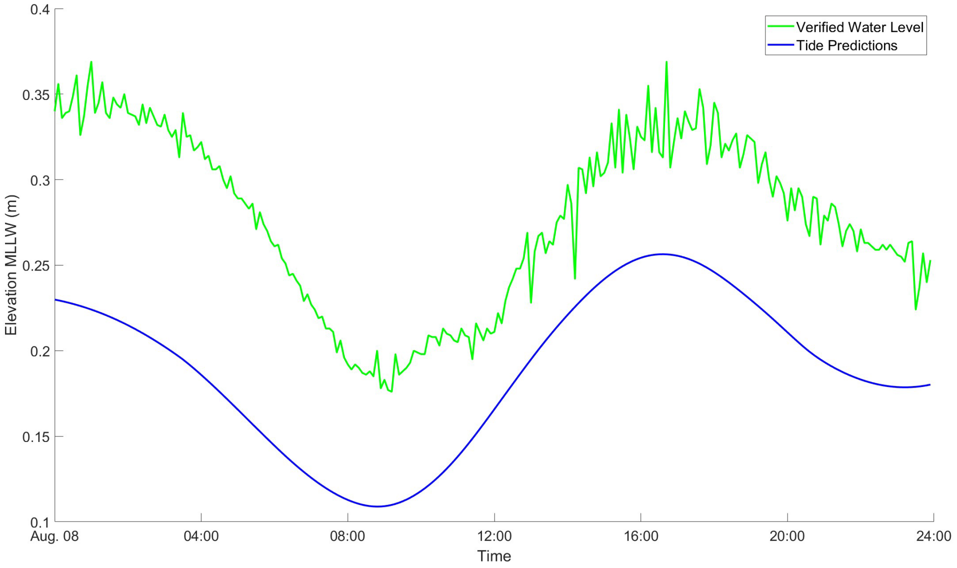

Figure 9. Predicted tide and Verified water levels measured at NOAA Station 8771013 for August 8th, 2024 (C2).

C3 on May 14, 2025 had no precipitation. As shown in Figure 10, the winds exceeded 10 m/s during the survey period. The tidal range was 48 cm, with a high tide of 0.69 m and a low tide of 0.2 m in reference to MLLW. The electrical conductivity of the water was 9.6 mS/cm (an electrical resistivity of 0.51 Ohm-m) during the survey period, shown in Figure 12. The information for Figure 10, Figure 11, and Figure 12 was provided by NOAA Station 8771013 (NOAA, 2025). A water sample taken from within the channel found a temperature corrected electrical resistivity to be 0.44 Ohm-m at 25°C, the same temperature as the water on the day of C3.

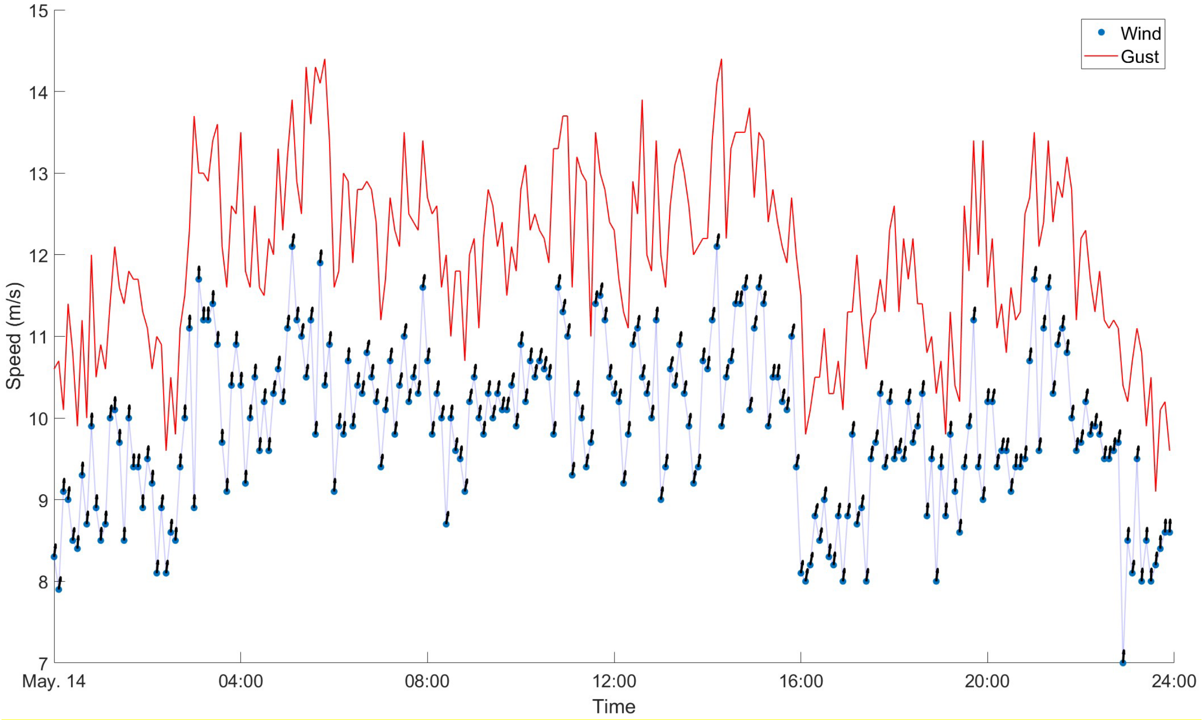

Figure 10. Wind speed and direction measured at NOAA Station 8771013 for May 14, 2025 (C3).

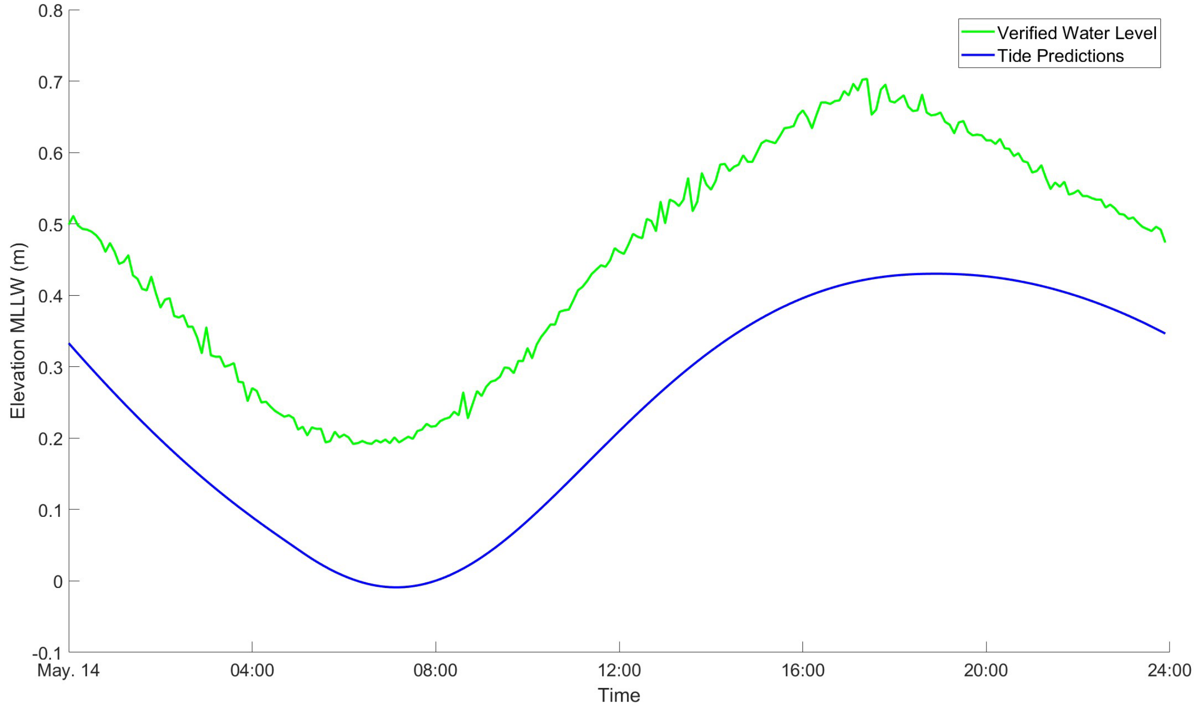

Figure 11. Verified and predicted water levels at NOAA Station 8771013 for May 14, 2025 (C3).

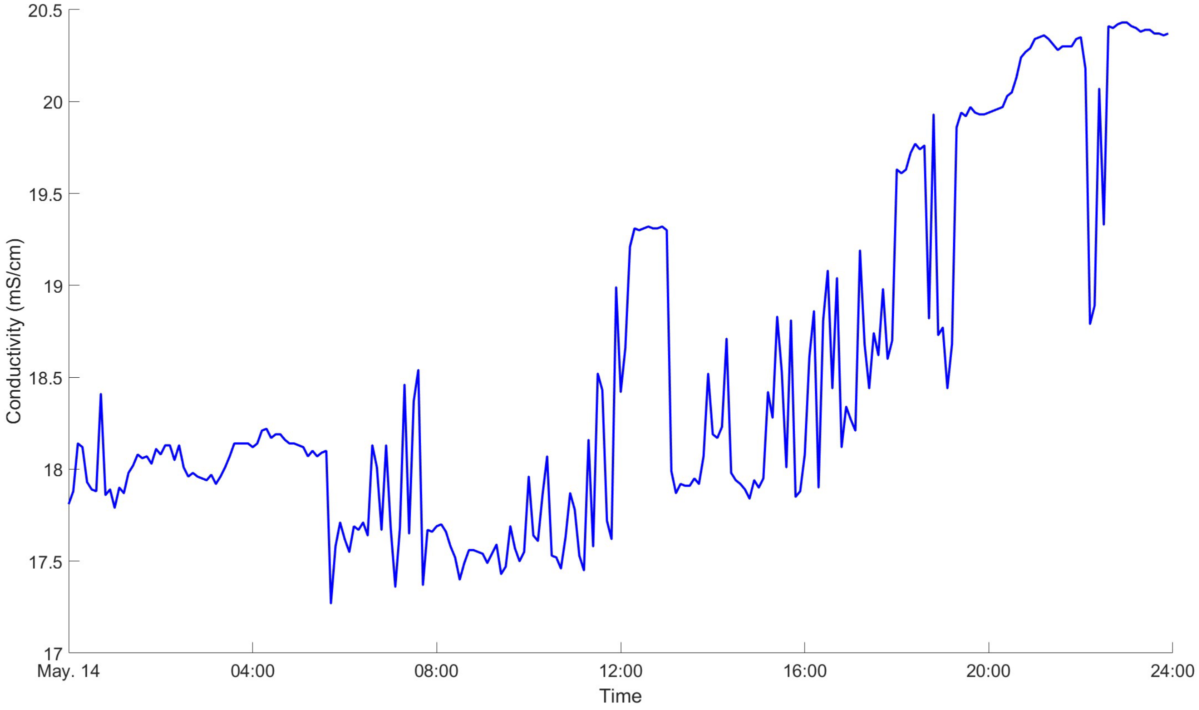

Figure 12. Conductivity in Ohm-m for NOAA Station 8771013 for May 14, 2025 (C3).

Oceanographic Measurements

During the field campaigns conductivity, temperature, and depth (CTD) data and water samples were collected. CTD data (vertical profiles) were collected using a CastAway CTD attached to a sinker line at several locations near the field site. Temperature and salinity data were used in the determination of acoustic attenuation coefficients with average values taken from a depth beyond the instrument's blanking distance (1.4 m depth). Depth-averaged measured temperature and salinity were 12.9°C and 15.2 psu, respectively, with profiles provided in Figure 13. Depth averages are used with the assumption that there is considerable vertical mixing during each vessel passing.

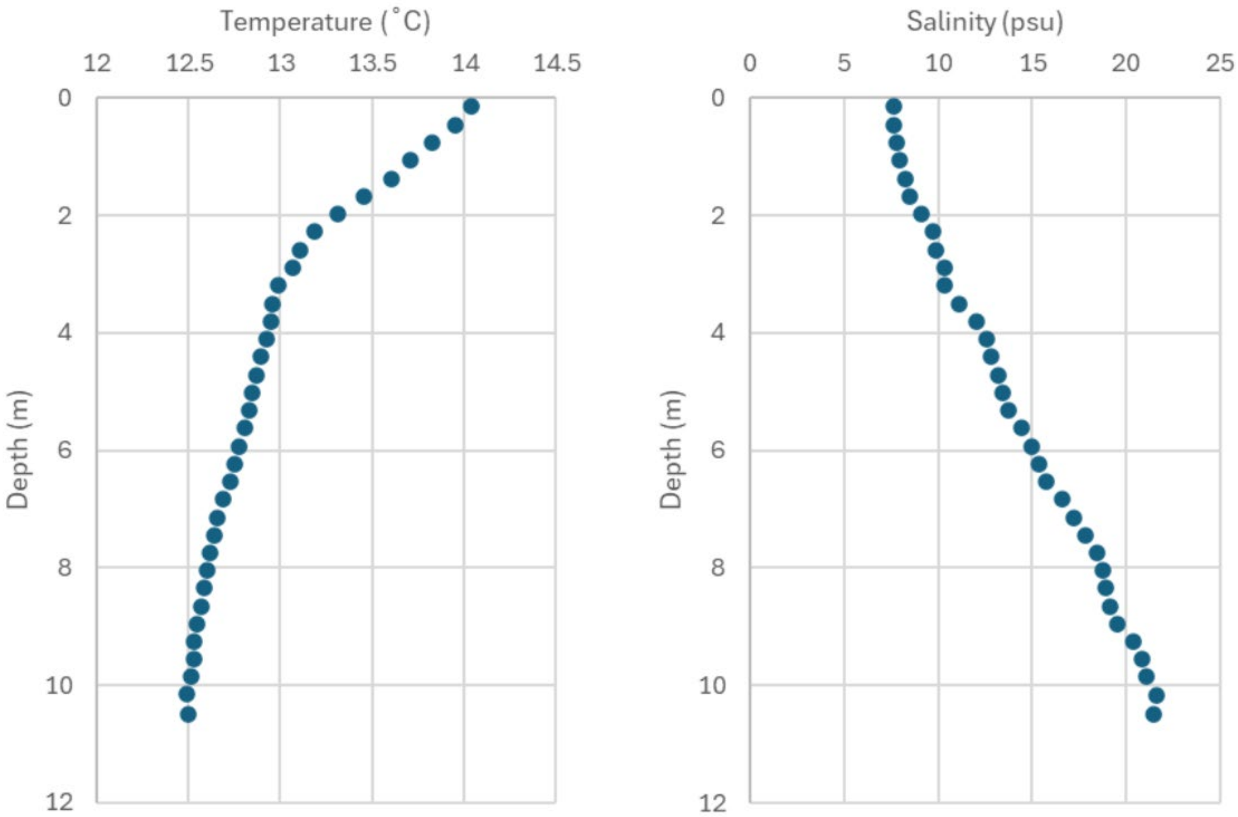

Figure 13. Water temperature (left) and salinity (right) profile over depth on January 30th, 2024 (C1) taken near 29.5407 °N, -94.902 °W.

Three water samples of approximately 20 Liters shown in Figure 14 were collected using a small pump to retrieve water from a depth of 1 m. Water sample one was collected within the HSC near 29.5407 °N, -94.902 °W, with the water depth being approximately 10.5 m, water samples two and three were collected 400 m from the green side of the channel near 29.5378 °N, -94.9063 °W. The locations of each water sample can then be correlated with specific background backscatter measurements.

Figure 14. Photo of water sample containers used during field deployments.

Through filtering the water in the laboratory, the total suspended solids were able to be weighed and a SSC value for each water sample was determined as shown in Table 1. Various volumes of water were filtered to prevent filters from clogging from the amount of total suspended solids.

Table 1: SSC values determined from collected water samples (C1)

Sample	**TSS (mg)**	**Volume (L)**	**SSC (mg/L)**
Control 1	0.03	1.5	0.02
1A	19.85	1.0	19.85
1B	10.90	0.5	21.80
2A	9.64	0.5	19.29
2B	9.72	0.5	19.45
3A	8.22	1.0	8.22
3B	6.46	0.5	12.91
Control 2	-0.10	1.0	-0.10

Note: TSS is mass of Total Suspended Solids

Estimating Suspended Sediment Concentrations from Acoustic Backscatter

With known SSC from the gravimetric analysis performed on water samples. A relationship between the SSC and the dB amplitude measurement can be established using the calibration coefficient “C” shown in (1). With C, the SSC can be determined for all the cells captured in the measurement using the recorded amplitude of the backscatter.

However, acoustic signals attenuate as they pass through any medium. With the backscatter data, the largest amplitude readings are recorded closest to the instrument trending to lower dB readings with increasing depth. To correct backscatter data, attenuation due to spherical spreading, energy lost to the medium, and energy loss due to the sound’s interaction with suspended solids are added back to the backscatter. First, the water-corrected backscatter (WCB) needs to be determined by scaling the raw backscatter, and accounting for spherical spreading and water attenuation. The WCB can be found using (2) given by Lohrmann (2001).

$$WCB = 0.43Amp + 20\log(R) + 2R\alpha_w \qquad (2)$$

Where 0.43 is the scaling factor given by Nortek, the company that produces the used acoustic instrument, to scale the raw backscatter to the measured backscatter, Amp is the raw backscatter, 20log(R) is the correction for spherical spreading found with the distance from the instrument R, and $2R\alpha_w$ is the correction for water attenuation with the water absorption coefficient α_w. Lohrmann (2001) provides various values of α_w for both fresh and saltwater obtained through experimentation with various instrument frequencies for Nortek instruments. However, to obtain a water absorption coefficient that best matches the environment in which the data were collected Equation (3) (Landers et al., 2016) is used.

$$\alpha_w = 8.69\left(\frac{SA_w f_T f^2}{f_T^2 + f^2} + \frac{B_w f^2}{f_T}\right)(1 - 6.54 \cdot 10^{-4} P) \qquad (2)$$

Where S is salinity in parts per thousand (ppt), A_w is the constant for ionic relaxation in sea water which is 2.34E-6, B_w is a constant for viscosity characteristic of pure water equal to 3.38E-6, f is the operating frequency of the measuring instrument (kHz), f_T is the temperature dependent relaxation frequency (kHz) which can be found via (4) (Landers et al., 2016), and P is the pressure (atm). At the maximum depth of the channel, which is approximately 16 m, the pressure term is approximately one so the effects of pressure can be ignored when finding the water absorption coefficient.

$$f_T = 21.9 \times 10^{\left[6-\frac{1520}{T+273}\right]} \tag{4}$$

Where T is the water temperature in degrees Celsius. To determine the water absorption coefficient that best represents the conditions in the HSC, CTD data should be used. By using the salinity and temperature values described in the Oceanographic Measurements section of this report, f_T is found to be 61.71 kHz, the water absorption coefficient is then found to be 0.026 dB/m. The WCB can then be determined using (2).

Plotting the WCB against the raw backscatter in Figure 15, the decrease over depth found in the raw backscatter no longer exists in the corrected backscatter which in contrast increases over depth. The increase in the WCB over depth indicates that suspended sediments do not significantly impact the signal. Therefore, it is unnecessary to correct the backscatter for sediment attenuation. Attempting to correct the WCB into a SCB may result in overcorrection or a flip in the concentration profile as some methods depend on the amplitude to decrease over depth. For higher concentrations that result in a decrease of backscatter amplitude across the sediment plume, it may be necessary to determine the SCB.

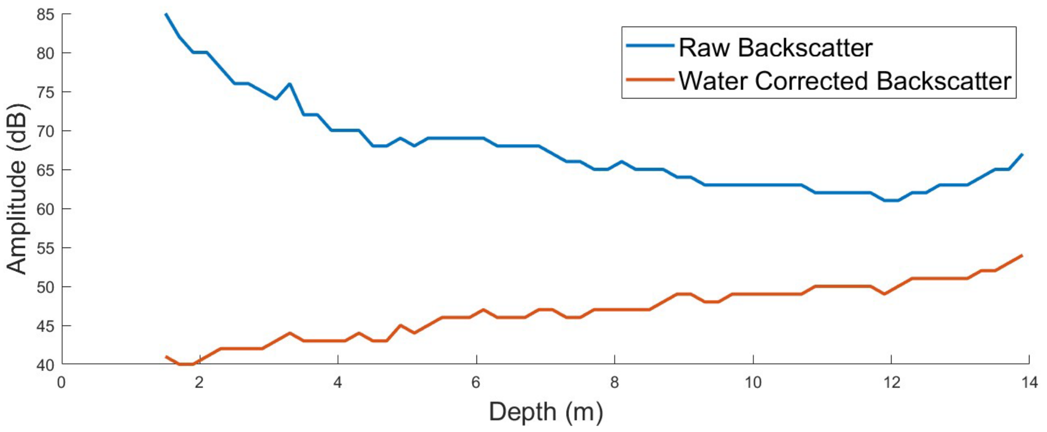

Figure 15. Comparison of Raw Backscatter (blue) and WCB (orange) with respect to water depth.

Finally, using the SSC determined from the gravimetric analysis along with the associated WCB, (1) can be used to determine C. Averaging the values of C determined using each background water sample, it is calculated that C = -2.976. This calibration factor is then used to determine the SSC of each measured cell.

Determining Bed Shear Stress

Quantifying the bed shear stress generated by passing vessels can give a better understanding of where in relation to the distance from the vessel and by how much does the shear exceed that of the critical bed shear stress. In this work the bed shear stresses are determined using qualities of the sediment. Measured velocities do not reach the bed but instead stop 10% above the total depth for each profile. Because of this, the velocity at the bed needs to be estimated using turbulent boundary layers. From Nikuradse (1933), the elevation above the bed for where shear velocities are 0 can be found by,

$$z_0 = \frac{\nu}{9u_*} \tag{5}$$

For smooth turbulent flow where u_* is the shear velocity, and

$$z_0 = \frac{k_n}{30} \tag{6}$$

For rough, turbulent flow where k_n is equivalent to the grain roughness which can be expressed as the grain diameter. By first assuming rough turbulent flow, a first iteration of calculations can be performed to determine if the flow is smooth turbulent. This is done as the friction factor can be explicitly calculated for rough turbulent flows and provides a good first guess for smooth turbulent iterations. Using the reference velocity u_r a distance z_r from the bed of the last data point measured the friction factor can be found by,

$$f_c = \left(4\log_{10}\left(\frac{z_r}{z_0}\right)\right)^{-2} \tag{7}$$

Using this friction factor to find the shear velocity,

$$u_* = \sqrt{\frac{f_c}{2}}u_c(z_r) \tag{8}$$

With this shear velocity, Madsen et al. (1993) showed that for fully rough turbulent flow the inequality (9) is true. Otherwise, if (9) is false, the flow is fully smooth turbulent flow.

$$\frac{k_n u_*}{\nu} \geq 3.3 \tag{9}$$

Where ν is the kinematic viscosity of the fluid. If it is found that the flow is smooth turbulence, z_0 can be recalculated using (5). Again, this can be plugged into (7) to find a new friction factor and then plugged into (8) to find a new shear velocity. These processes can be repeated until the change in the shear velocity falls below some accuracy threshold. Once the final shear velocity is determined, the bed shear stress can be found by,

$$\tau = \rho(u_*)^2 \tag{10}$$

where ρ is the density of the fluid. The bed shear stress can then be compared to the critical shear stress. If the bed shear exceeds the critical shear stress, then sediment motion will occur.

Determining Vorticity

By calculating the vorticity of the flow, larger scale rotations or eddies produced by the propeller wash can be identified. Vorticity is the curl of the velocity field which can be found by,

$$\omega = \nabla \times u = \left(\omega_x, \omega_y, \omega_z\right) = \left(\frac{\partial w}{\partial y} - \frac{\partial v}{\partial z}, \frac{\partial u}{\partial z} - \frac{\partial w}{\partial x}, \frac{\partial v}{\partial x} - \frac{\partial u}{\partial y}\right) \tag{11}$$

where w is the vertical velocity, v is the velocity moving across the channel, and u is the velocity moving along the channel. By using a fixed step size for each axis determined by the mean distance between each point such that dx = 34.7 cm, dy = 7.63 cm, and dz is fixed in the equipment set up at 20 cm.

Propeller Wash Data Collection

The sediment plume generated by a passing vessel's propeller wash is quantified through the acoustic backscatter amplitude recorded by the survey vessel-mounted ADCP. The survey vessel remained outside of the main channel until a vessel entered the survey area. Once a vessel began passing, the direction, vessel type, name, callsign, Maritime Mobile Service Identity (MMSI), and approximate draft were recorded. Once the survey vessel had positioned itself and it was safe to cross the channel, multiple transects were made across in a snaking pattern attempting to stay close to the first transect of that vessel measurement. Multiple vessels encountered in the same measurement had all their information recorded, small fishing vessels that did not have Automatic Identification System (AIS) active were not identified. All AIS data were retrieved from the Bureau of Ocean Energy Management - BOEM and the National Oceanic and Atmospheric Administration - NOAA (2024), as well as BOEM and NOAA (2025) for the corresponding day of each survey

Relevant collected data from the vessel-mounted ADCP include survey vessel track, acoustic backscatter amplitude, and depth profiles of current velocity. These are the main raw data used for analysis of propeller wash. The survey vessel track is a plot of the instrument’s latitude and longitude recorded at each point a measurement is collected using the GNSS antenna. This can be used to compare the distance from the survey boat to the measured vessel using its AIS location data. Along with this, points can be plotted as in Figure 16 to visualize the path that the survey vessel took during the measurement.

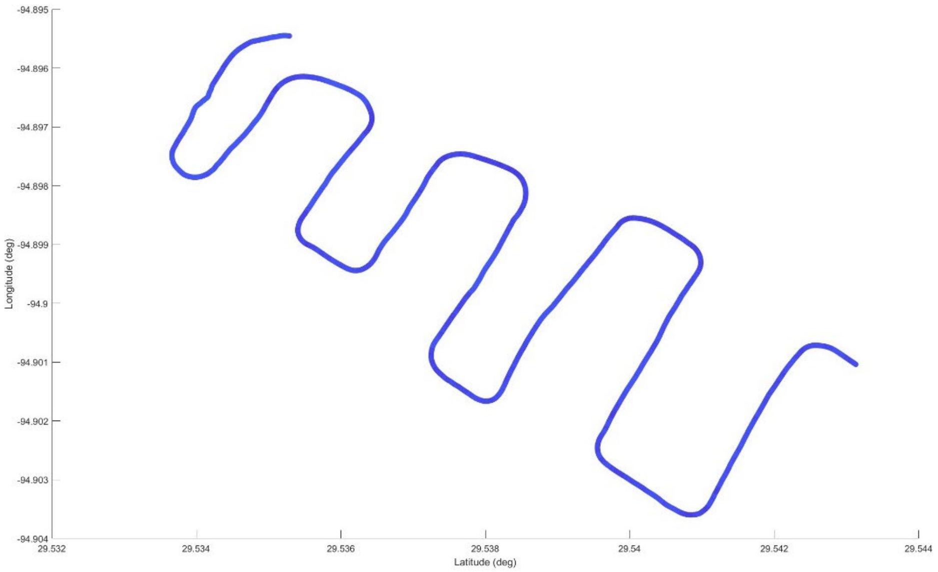

Figure 16. Example survey track traveled during a measurement.

Backscatter amplitude measurements are recorded in units of dB and are collected through four of the instrument’s acoustic transducers. The backscatter amplitude provides the instrument with the strength of the returning signal which can change based on the distance and type of media the sound wave passes through. An example of the raw backscatter amplitude is shown in Figure 17. The data are plotted as depth on the y-axis and time along the x-axis. The color bar shown on the left indicates the amplitude of the acoustic signal. The solid yellow line indicates the estimated depth of the bed, and the dotted line is 90% of the depth. The data beyond 90% depth can be significantly degraded due to various forms of acoustic interference therefore they are disregarded to avoid inaccurate results.

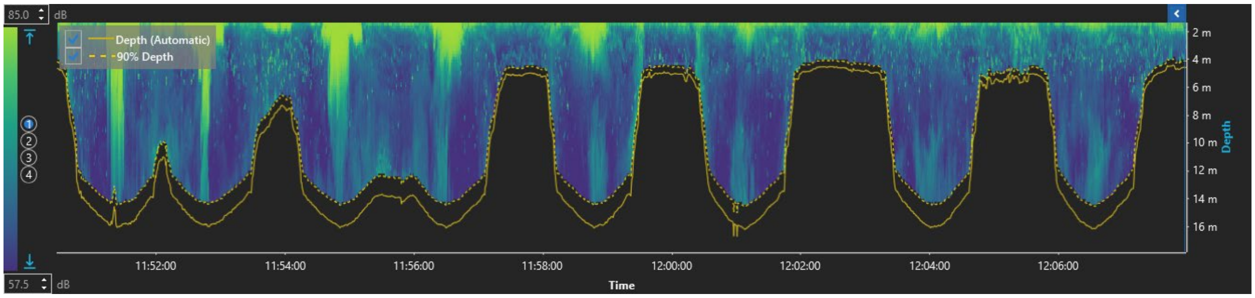

Figure 17. Example backscatter amplitude profile time series highlighting the 10% of depth data gap at the bed from Signature VM Review plots.

The recorded current profiles and their direction are determined by using the same four transducers used in recording the backscatter. The Doppler shift determined through the four beams is used to calculate the current velocity and direction throughout the water column. An example of the magnitude of the velocity is shown in Figure 18. Similar to the backscatter data, this is shown with depth along the y-axis and time along the x-axis. The color bar indicates the magnitude of the velocity in m/s.

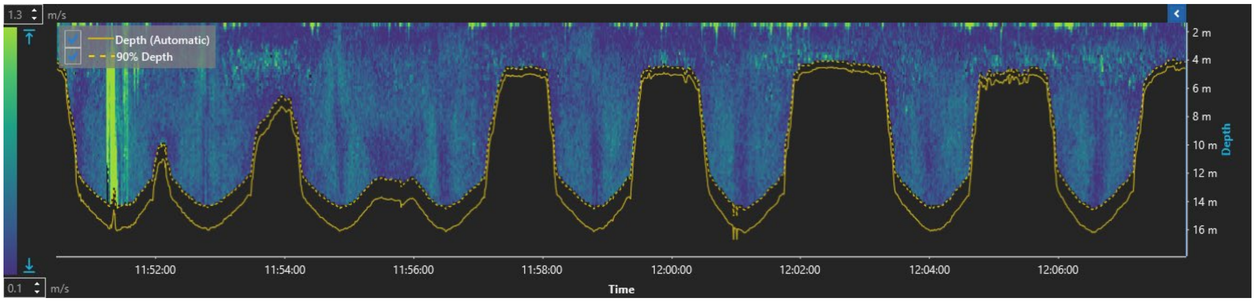

Figure 18. Example current profile time series from Signature VM Review application.

As vessels were encountered in the field, basic notes were recorded using available AIS data and visual observations. Information that was not readily observed or missed due to multiple passing vessels was later obtained using AIS data. Summaries of all vessels captured during C1, C2, and C3 are given in Table 2, Table 3, and Table 4, respectively. In addition, the corresponding photo, speed, dimensions, track, and recorded measurement plots for each vessel are tabulated in

Appendix A. Examples of these data are shown for the containership MAIPO (Figure 19) and for the tugboat BROWN WATER VII (Figure 20), respectively.

Table 2: Vessels contributing to measured data in C1.

#	Vessel name	MMSI	Vessel type	Direction
1	SEA PANTHER	241618000	Oil tanker	Inbound
2	HAFNIA LEO	256448000	Oil/chem tanker	Outbound
3	PLUTO MOON	636019310	Crude oil tanker	Inbound
4	PHILLIP	367003780	Tug	Outbound
5	MOL COURAGE	431296000	Container ship	Outbound
6	STOLT EFFICIENCY	319488000	Oil/chem tanker	Inbound
7	RF STELLA	256764000	Oil/chem tanker	Inbound
8	BOW AQUARIUS	257384000	Oil/chem tanker	Outbound
9	CREOLE SUE	367005520	Tug	Outbound
10	NEAL J SEAGO	367524270	Tug	Outbound
11	SHERGAR	565355000	LPG tanker	Inbound
12	BELLE AMIE	367649360	Tug	Inbound
13	CAPT DUB ALLEN	368140540	Tug	Outbound
14	SAMMY TATE	367551680	Tug	Inbound
15	AZTEC	372111000	Oil tanker	Outbound
16	C J BOYNE	367005270	Tug	Inbound
17	ALAM SAYANG	353511000	Bulk carrier	Inbound
18	EPIC SAMOS	563005200	LPG tanker	Inbound
19	CMA CGM MELISANDE	256888000	Container ship	Inbound
20	CAPT DAVID CARRIERE	367709930	Tug	Outbound
21	NCC NOOR	403512001	Oil/chem tanker	Inbound
22	MATTHEW	367688580	Tug	Outbound
23	MIKE HOWARD	368103560	Tug	Inbound
24	MARTIN EXPRESS	366884150	Tug	Outbound
25	BRENTHOLMEN	538005553	Oil/chem tanker	Inbound
26	BUD SONIER	367415180	Tug	Inbound
27	MICHELLE ELISE	368339380	Tug	Outbound
28	CHRISTIAN REINAUER	366832740	Tug	Outbound
29	DOUGLAS MURPHY	367511270	Tug	Inbound
30	NED BROOKS	368214730	Tug	Outbound
31	BROWN WATER VII	367007540	Tug	Inbound
32	AMANI	636022462	Bulk carrier	Outbound
33	BALLA	636021796	Crude oil tanker	Inbound
34	DJP II	368068030	Tug	Inbound
35	SC SCORPIO	477100700	Oil/chem tanker	Outbound

Table 3: Vessels contributing to measured data in C2.

#	Vessel name	MMSI	Vessel type	Direction	#	Vessel name	MMSI	Vessel type	Direction
1	CLIPPER MOON	258929000	Tanker	Outbound	17	FANNIN	368027210	Tug	Inbound
2	LONDON EXPRESS	310765000	Container ship	Outbound	18	MARGARET K	368199740	Tug	Inbound
3	NISI LIMASSOL	209848000	Tanker	Inbound	19	TEXAS RESPONDER	366595000	Pollution control	Outbound
4	STENA PROVIDENT	210325000	Tanker	Inbound	20	CHEM SPICA	636022066	Tanker	Inbound
5	LILAC RAY	636019637	Tanker	Inbound	21	FATHER PAT	367519320	Tug	Outbound
6	HB GOLDEN EAGLE	538008758	Bulk carrier	Outbound	22	MATTERHORN EXPLORER	636020880	Tanker	Inbound
7	KEEGAN NO.1	563110500	Tanker	Inbound	23	GOOD SHEPHERD	367332950	Tug	Inbound
8	JOSSET	366841020	Tug	Inbound	24	KAZAK	565516000	Tanker	Inbound
9	DOLPHIN	367401290	Tug	Inbound	25	FORKED ISLAND	367688280	Tug	Inbound
10	LLANO	367506740	Tug	Inbound	26	HAMPSHIRE	636013336	Tanker	Inbound
11	VIVIT DUBHE	636018565	Tanker	Outbound	27	PATI R MORAN	367445000	Tug	Inbound
12	RADIANT PRIDE	636018722	Tanker	Outbound	28	GREEN PLANET	636016290	Tanker	Inbound
13	ETHANE PEARL	538006977	Tanker	Inbound	29	BELL	368085790	Tug	Inbound
14	N/A	N/A	Tug	Outbound	30	STOLT BRELAND	319017500	Tanker	Outbound
15	MSC LOS ANGELES	636021449	Container ship	Inbound	31	DOLPHIN	367401290	Tug	Outbound
16	MAIPO	636092848	Container ship	Inbound	32	UOG DESPINA V	636014609	Tanker	Inbound

Table 4: Vessels contributing to measured data in C3.

#	Vessel name	MMSI	Vessel type	Direction
1	MERLE GONSOULIN	367750650	Tug	Inbound
2	SEABULK CHALLENGE	303104000	Tanker	Outbound
3	CYNTHIA K	368099320	Tug	Outbound
4	COLT CLARY	367571770	Tug	Outbound
5	JONES	368047580	Tug	Inbound
6	MSC_N/A	N/A	Container	Inbound
7	SUNNY PHOENIX	311001244	Container	Inbound
8	STOLT ACHIEVEMENT	319446000	Tanker	Outbound
9	SELENKA	249598000	Tanker	Inbound
10	AXIS	368099430	Supply	
11	BOW CARDINAL	538009779	Tanker	Inbound

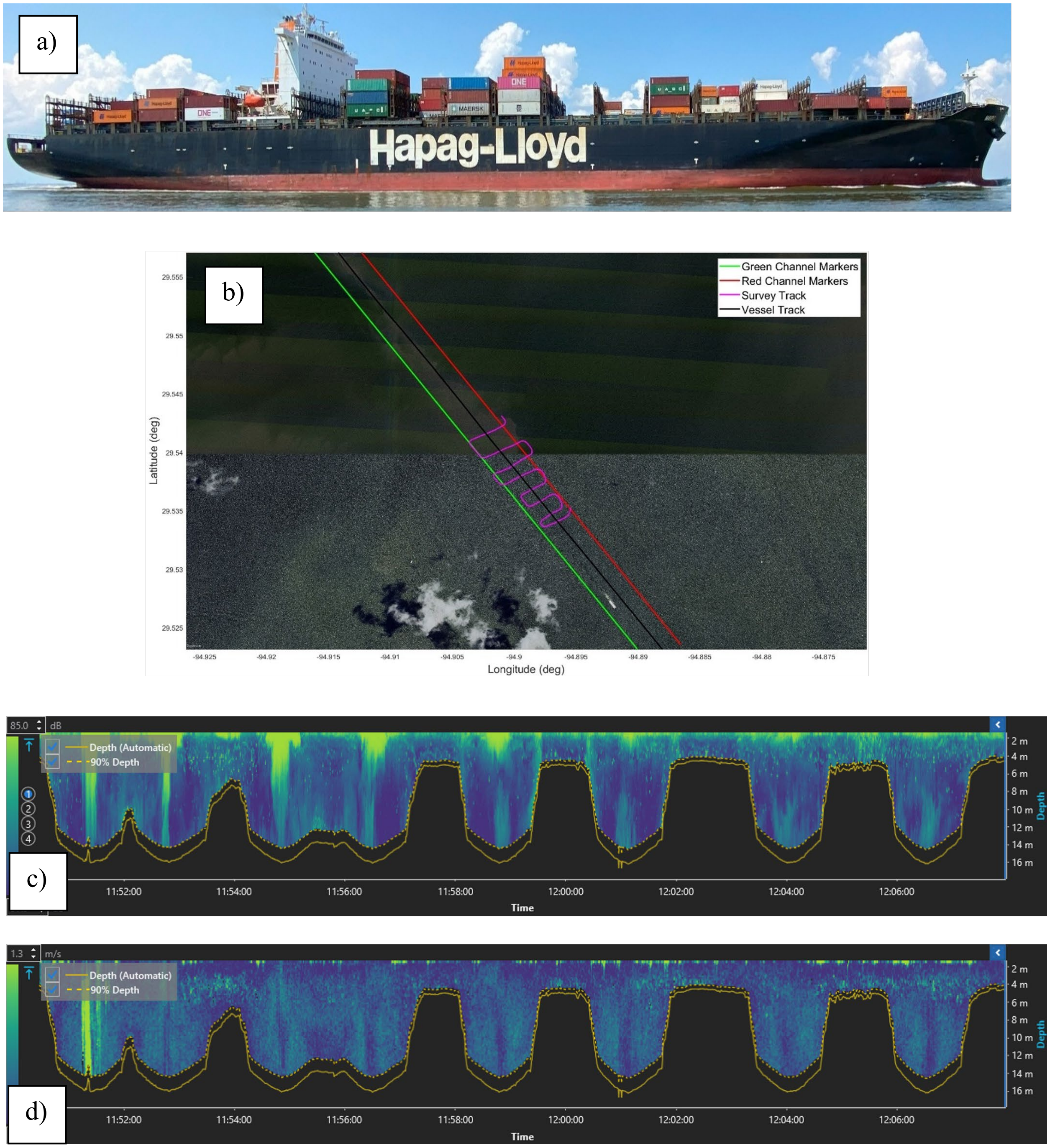

Figure 19. Vessel MAIPO (Speed: 10.9 kn, Length: 306 m, Breadth: 40 m, Draft: 10.7 m). Panel a): Photo of vessel. Panel b): Survey vessel track. Panel c): Raw acoustic backscatter profile data along timed survey vessel track. Panel d): Measured water velocity profile data along timed survey vessel track.

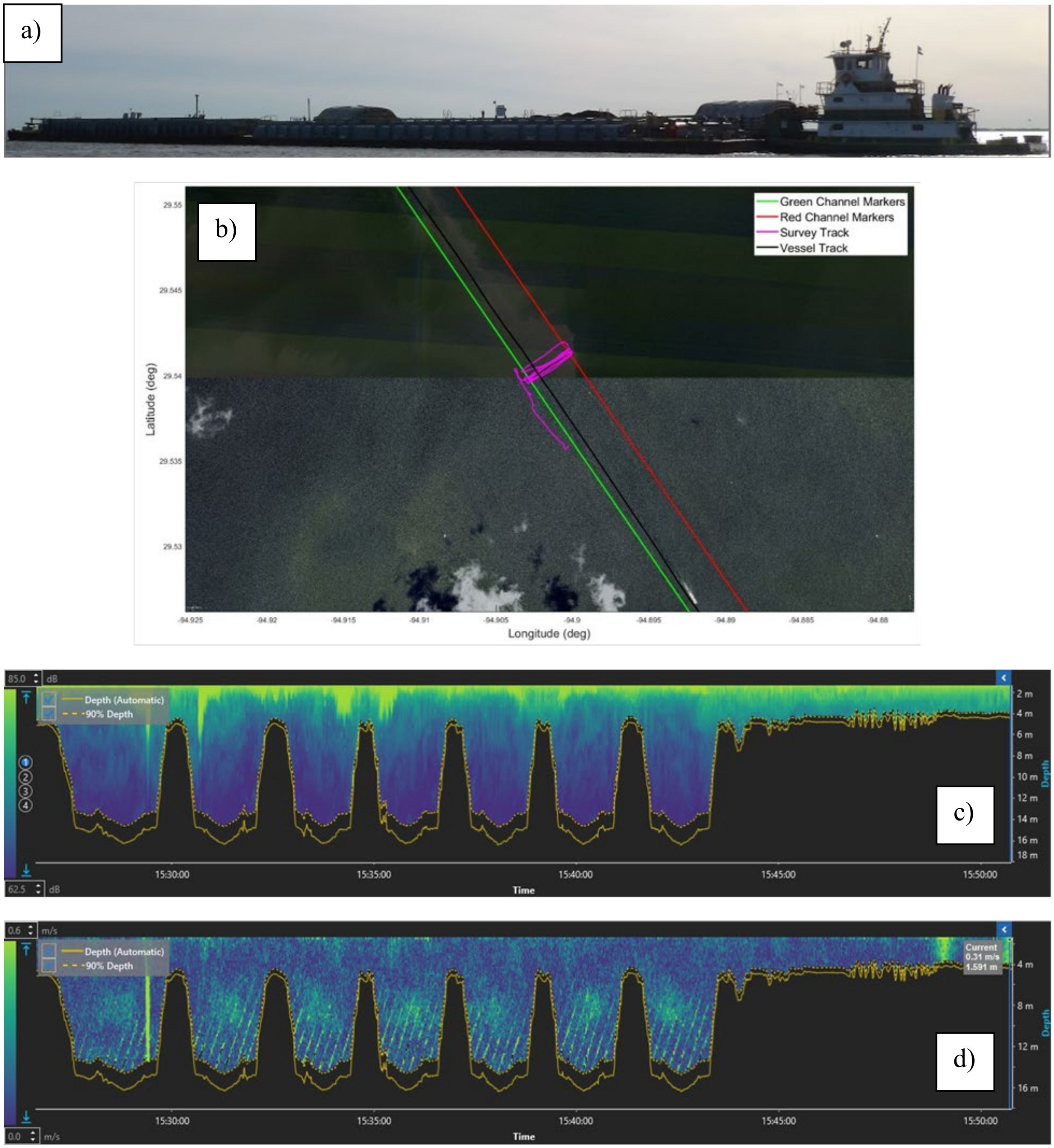

Figure 20. Vessel BROWN WATER VII (Speed: 5.29 kn, Draft: 2.9 m). Panel a): Photo of vessel. Panel b): Survey vessel track. Panel c): Raw acoustic backscatter profile data along timed survey vessel track. Panel d): Measured water velocity profile.

Electrical Resistivity Data Collection and Post-Processing

The electrical resistivity of the water column behind deep draft vessels was measured using a SuperSting R8 electrical resistivity meter and 150 m long towed cable, manufactured by Advanced Geosciences Inc. (AGI). The SuperSting was onboard the survey vessel and was powered by a EU1000i Honda generator. An onboard GPS provided the SuperSting with location data while a transducer was mounted on the starboard side of the vessel and provided the SuperSting with water depth and water temperature data, both powered by a 12-volt car battery. The towed cable was tethered to the survey vessel from a beam which extended approximately 1 m over the starboard edge. A built-in anchor point 10 m from the SuperSting connector on the towed cable allowed for safe towing of the cable through the survey site. The first current electrode was spaced 30 m after the anchor point to ensure that the survey vessel's wake did not interfere with measurements. The second current electrode and nine potential electrodes were spaced 10 m apart on the remaining 110 m of the towed cable from the first current electrode. Figure 21 shows a simplified arrangement of the equipment onboard the survey vessel. Pool noodles were securely fastened with zip ties approximately 1 m ahead and the potential electrodes, ensuring that the electrodes remained fully submerged while near the water surface. After the last potential electrode, a large buoy was attached to add extra buoyancy and for visual location of the end of the towed cable.

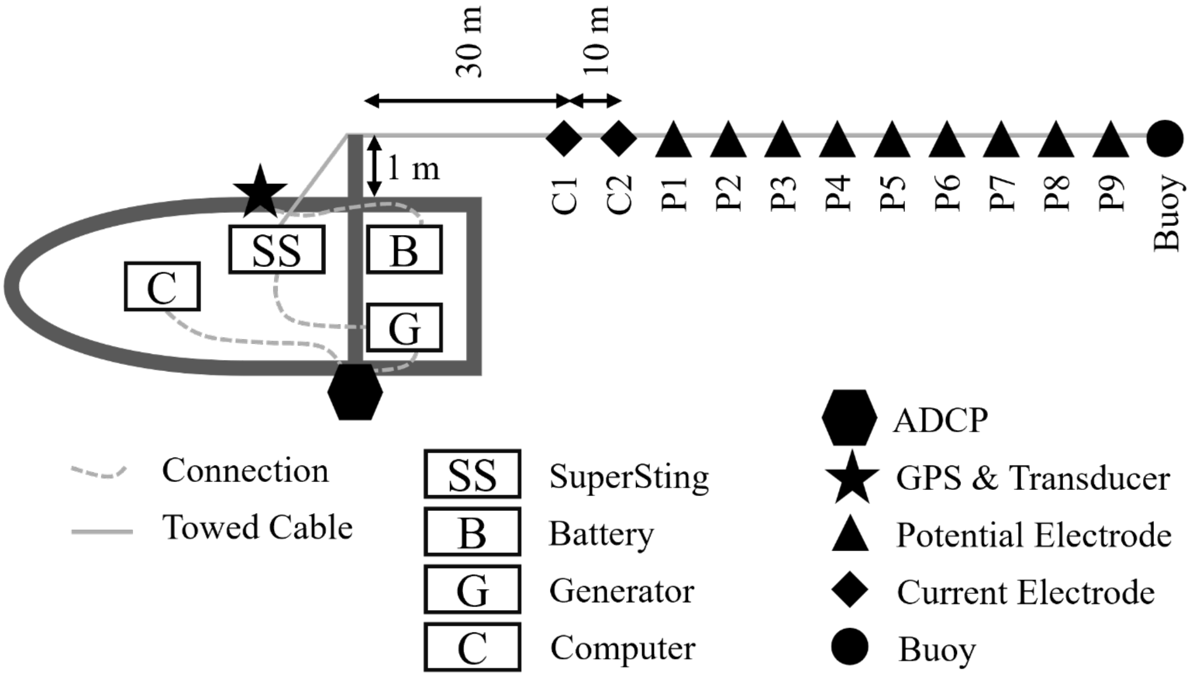

Figure 21. Simplified model of survey equipment onboard the survey vessel, not to scale.

The arrangement of the current and potential electrodes on the towed cable creates a dipole-dipole electrode array (Edwards, 1977). In a dipole-dipole array, the spacing between the current electrodes (referred to as electrodes A and B) are equal to the spacing between the potential electrodes (referred to as electrodes M and N), where the electrode spacing, *a*, is 10 m on the towed cable. The spacing between the current and potential electrode pairs is *na*, where *n* is the number of electrode spacings (Edwards, 1977). In land-based electrical resistivity tomography surveys using a dipole-dipole array, the location of the measurement shifts along the electrode cable by changing which electrodes to inject current and measure voltage potentials; the spacing also increases by increasing *n* (Binley, 2015). However, the towed cable shown in Figure 19 changes measurement location through towing the entire cable behind the survey vessel, rather than changing the current or potential electrodes. A common representation of the measured data are seen in a pseudosection as shown in Figure 22, which is useful for visualization of the data, though it is not an accurate representation for the spatial distribution of the measured data (Edwards, 1977 and Everett, 2013).

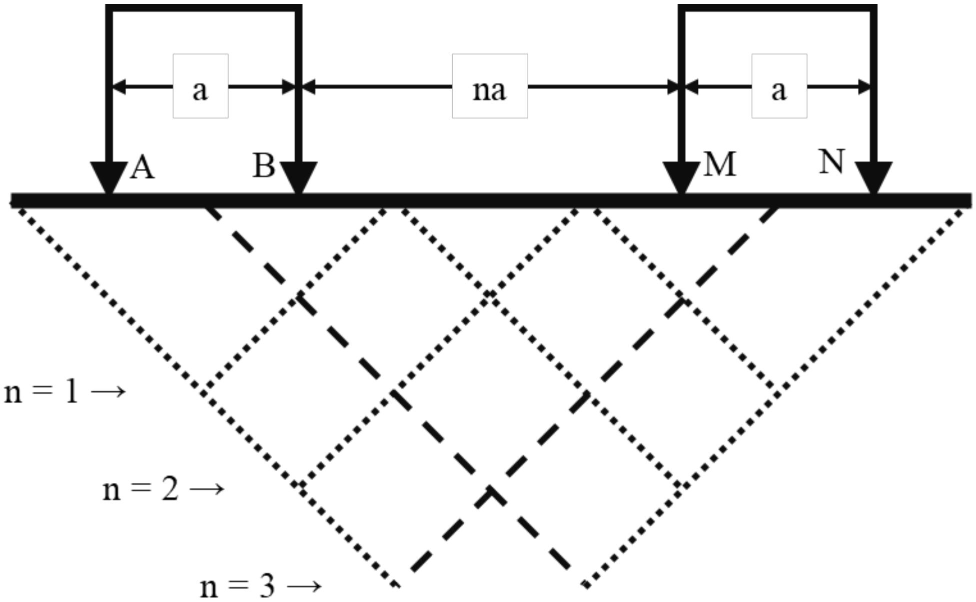

Figure 22. Four electrode dipole-dipole array.

Field measured electrical resistivity data are not assumed to be the true resistivity of the subsurface at a point. The collected field data are apparent electrical resistivity values, where it is assumed that the entire subsurface is homogeneous (Everett, 2013). In reality the subsurface is not homogeneous and therefore these data must be inverted to obtain the true electrical resistivity distribution. Apparent resistivity is given by

$$\rho_a = \kappa \frac{V}{I} \tag{12}$$

where, ρ_a is the apparent resistivity, V is the voltage potential, and I is the injected current (Everett, 2013). The parameter κ, in the above equation, is the geometric factor which is dependent on the physical spacing of the current and potential electrodes. For the dipole-dipole array shown in Figure 22,

$$\kappa = \pi n(n+1)(n+2) \tag{13}$$

where n is the number of electrode spacings between the current and potential electrode pairs (Everett, 2013).

Figure 23 shows the pseudosection for the towed cable as the survey vessel traverses the survey area. As seen in Figure 23, the movement of the survey vessel causes the pseudo section to form a left-leaning-parallelogram. The two electrodes nearest the survey vessel are the current electrodes (denoted as diamonds) and the remaining nine are the potential electrodes (denoted as triangles). Each horizontal row of measurement points (denoted as circles) comprises a channel. The SuperSting has eight channels and can record up to eight data points per current injection, seen as a diagonal slice of measurement points. As the vessel travels forward, new measurements are taken, adding more data points to the left of existing data. At the same time, location data are collected by the onboard GPS and water depth and temperature are measured by the onboard transducer. After data collection is complete, the field electrical resistivity values are aligned with the GPS and transducer using AGI's SuperSting Manager app. Once the data are aligned, two files are created which can be post-processed in AGI's 2D EarthImager software. The first file contains the electrical resistivity data collected from the field and the second file contains the GPS location, water depth, and water temperature data. Surveys which were transverse to the HSC were trimmed to the HSC's boundary and surveys conducted longitudinally within the HSC were trimmed to a maximum length of 265 m. All trimmed survey sections are straight, removing effects caused by the survey vessel turning. This trimming process caused the pseudosection of the marine surveys (seen in Figure 23) to adopt a shape more commonly found on land (Figure 22), reducing post-processing error. The new, trimmed psedudosection shape is shown by the dashed line boundary in Figure 23. A total of nine surveys were created from the trimming process, listed in Table 5. Electrical resistivity data were collected in C2 and C3, however C2 data were not analyzed as the equipment was damaged during the campaign.

The surveys were processed in AGI's EarthImager 2D inversion software. The software uses both forward and inverse modeling approaches to generate an electrical resistivity distribution of the water column from the measured apparent resistivity values. The generalized Poisson equation (Nagel, 2012), is

$$\nabla \cdot [\epsilon(\boldsymbol{r})\nabla V(\boldsymbol{r})] = -\frac{\rho(\boldsymbol{r})}{\epsilon_0} \qquad (14)$$

where, $\epsilon(r)$ is the dielectric constant as a function of a position vector in space, $\boldsymbol{r}$. The parameter ϵ_0 is the permittivity of free space set as $8.554\text{x}10^{-12}$ F/m.

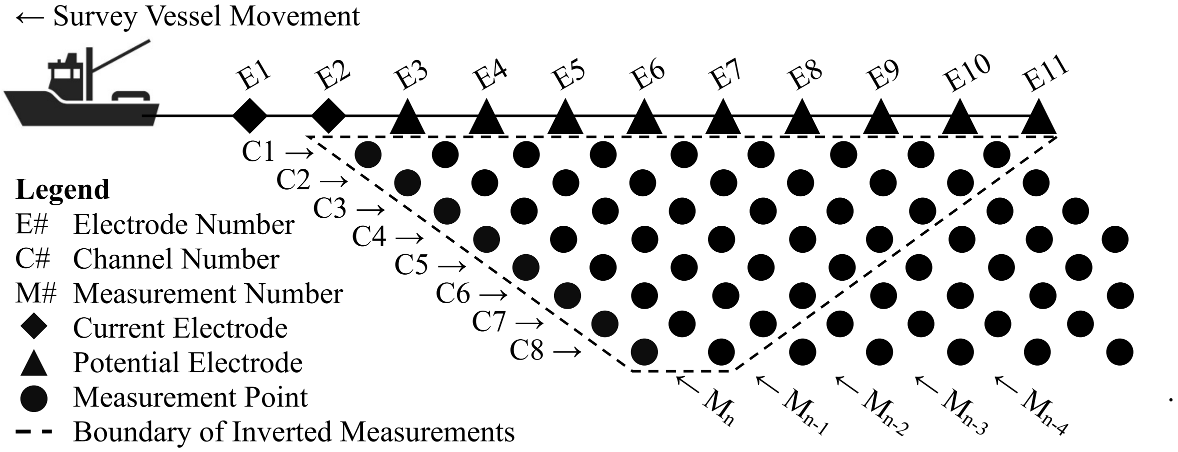

Figure 23. Apparent electrical resistivity pseudo-section, not to scale. Towed electrode cable shown behind survey vessel, moving left. E1 and E2 are current transmission electrodes, the remaining electrodes are used for voltage potential. The collected measurements are shown by solid circles with channel number increasing with depth and measurement number increasing to the left. Data outside the boundary of inverted measurements are not used for post-processing.

The voltage potential function is given as $V(\boldsymbol{r})$ and the charge density function is $\rho(\boldsymbol{r})$. The generalized Poisson equation is solved using a partial differential equation within the forward model using the finite difference method.

Table 5. Survey name, orientation, presence of vessel, channel depth and vessel from C3 for each survey compared for electrical resistivity surveys.

Survey Name	**Survey Orientation w/r to HSC**	**Presence of Vessel**	**Channel Depth* (m)**	**Length (m)**	**C3 Vessel #**
(S1)	Parallel	No Vessel	12.7	204	
(S2)	Parallel	Vessel	15.8	202	10
(S3)	Transverse	Vessel	15.8	240	2 & 3
(S4)	Parallel	Vessel	15.3	241	9
S5	Transverse	No Vessel	15.8	261	
S6	Transverse	Vessel	15.8	218	11
S7	Parallel	No Vessel	12.7	196	
S8	Transverse	Vessel	15.9	265	1
S9	Transverse	Vessel	15.7	232	6

*Depths for surveys which are parallel represent average depth over survey length, depths for surveys which are perpendicular represent max channel depth

In the inversion process first, a synthetic data set is created from the average of the measured electrical resistivity values; this forms the calculated apparent electrical resistivity distribution section. Then, the "true" inverted electrical resistivity distribution is created with an inverse damped least-squares optimization. Alignment of the calculated model and measured data are checked with the root mean square error (RMS) and L2-Norm. The RMS and L2-Norm are calculated as,

$$\mathrm{RMS} = \sqrt{\frac{\sum_{i=1}^{N}\left(\frac{d_i^{\mathrm{pred}} - d_i^{\mathrm{meas}}}{d_i^{\mathrm{meas}}}\right)^2}{N}} \tag{15}$$

$$\mathrm{L2-Norm} = \sum_{i=1}^{N}\left(\frac{d_i^{\mathrm{calc}} - d_i^{\mathrm{meas}}}{w_i}\right)^2 \tag{16}$$

where d_i^{pred} is the predicted data, d_i^{meas} is the measured data, d_i^{calc} is the calculated data, N is the number of apparent resistivity measurements, and w_i is the data weight used for L2-Norm. L2-Norm is then normalized by the number of apparent resistivity data. If the desired RMS and L2-Norm values have not been reached, the process iterates by recalculating the synthetic data using the forward model, then produces a new set of calculated electrical resistivities through inversion. Data processing is considered complete when the RMS is near the estimated noise, a user estimated percentage of the measured data, of the data set and the normalized L2-Norm is near unity (Zhou et al, 2014). The RMS describes the average error over the entire inverted data set, thus individual high-error measurements can inflate the overall RMS of the inversion. This may cause EarthImager to continuously iterate through the forward and backward models. To prevent this, systematic removal of the high-error data points is required. Wiese et al. (2015) conducted numerical experiments on an anisotropic domain using an inversion method which assumes isotropy and found that even when RMS was around ten times the noise of the model (an RMS of 20%), that the shape and location of anomalies are still observable. An additional control over inversion quality is the maximum number of iterations. The inversions presented herein were allowed up to eight iterations, as proposed by the inversion software, though the most iterations for the surveys in Table 5 was three. The result of the process is a 2D image of the true electrical resistivity distribution of the water column.

Further post processing was done to analyze the results of the surveys shown in Table 5. The average electrical resistivity of the water column with respect to depth was found to compare surveys with and without the presence of deep draft vessels. The statistical distributions of the water column electrical resistivity distributions were compared using the two sample non-parametric Kolmogorov-Smirnov (KS) statistical test. The KS compares sample distributions and looks for changes in shape, spread, and median without assuming a prior distribution or requiring normality and equal variance (Berger and Zhou, 2014). The KS tests were performed at the 0.05 significance level where rejection of the null hypothesis indicates that the sample distributions are significantly different. The differences in the sample distributions are attributed to the presence of resuspended sediments from deep draft vessels.

RESULTS

Water Velocity

Each measurement captured velocity profiles across space and time. Analysis results and comparisons with theoretical predictions are presented here using an example vessel passage during C2 (UOG DESPINA V). For this vessel we were able to conduct 13 channel crossings without any interference from other passing vessels. The measured velocities in the lee of the passing vessel are shown in Figure 24. The velocities shown capture both the propeller jet pushing water away from the vessel as well as the pull of water due to the vessel hull. In channel passing 1, the entire water column is moving twoards the vessel with a maximum velocity of approximatly 0.9 m/s. Opposite to this, in the 2nd passing, the velocities generated by the propeller are dominant, and push the water at a maximum velocity of 0.94 m/s. As time passes from the initial vessel crossing, the impacts of the vessel hull and propeller jet diffuses and results in the maximum velocity decelerating at approximately 4 cm/s^2. This is a result of how the jet spreads from its initially thin width of 25 m into later sections filling the channel with widths of approximately 145 m. However, once the velocity profile spreads to the width of the channel, the deceleration of the velocity reduces and the maximum velocity both due to the velocity jet and hull remains near 0.5 m/s.

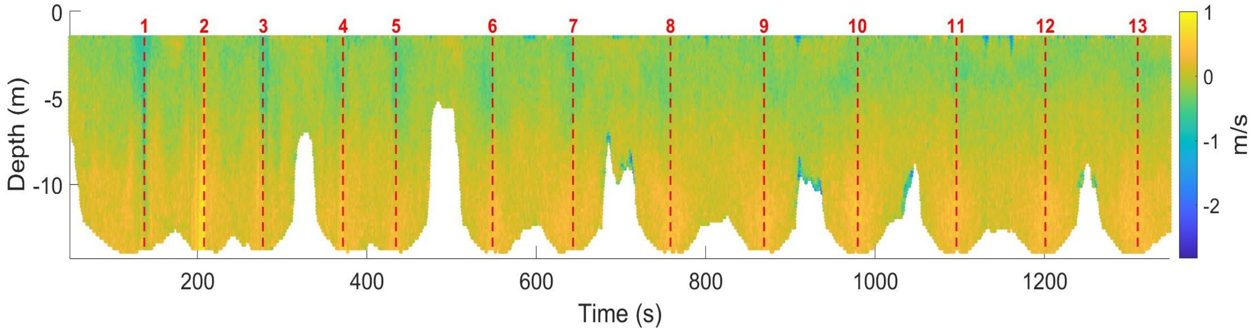

Figure 24. Measured velocity parallel with the channel produced by vessel UOG DESPINA V. Positive velocities (yellow) indicate flow moving away from the vessel negative velocities (blue) are moving towards the vessel.

Within each channel cross-section a maximum velocity can be picked out, and its corresponding time step can be used to separate its vertical profile. The vertical profiles of the thirteen channel crossings are plotted in Figure 25.

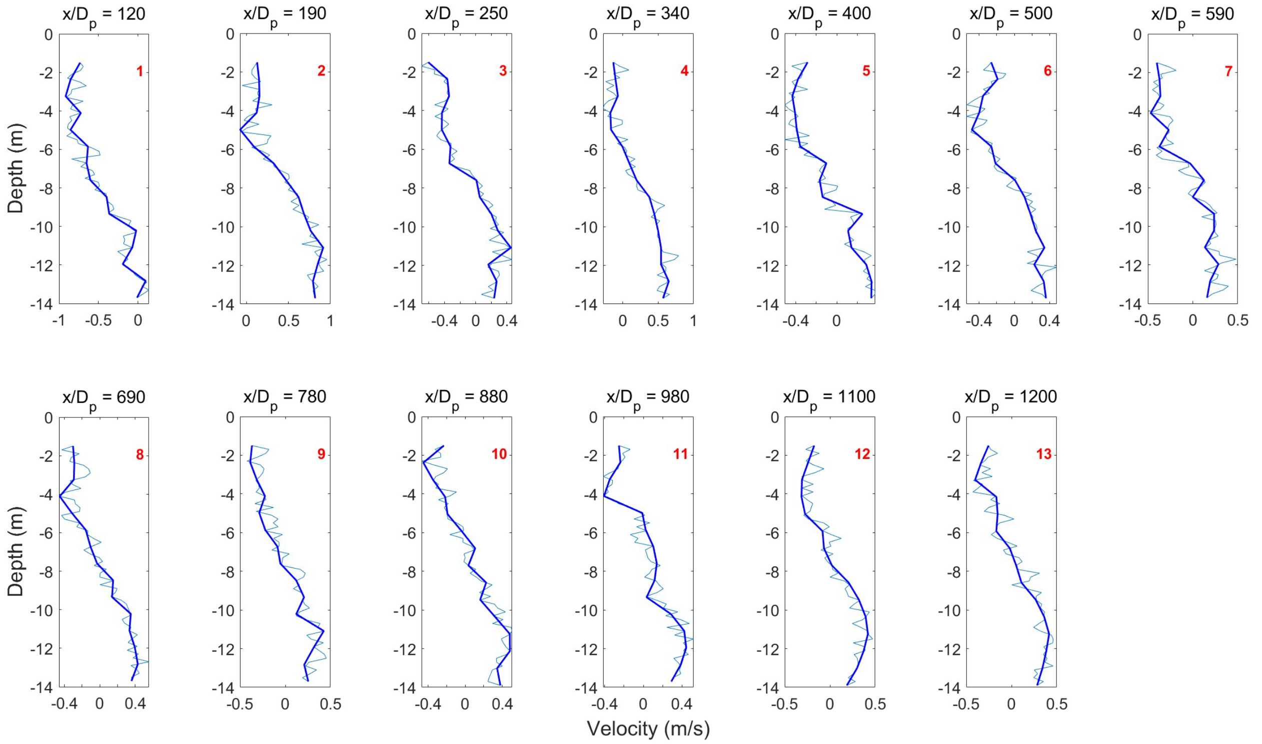

Figure 25. Select velocity profile transects produced by vessel UOG DESPINA V. Light blue line shows measured velocities while the dark blue line is the smoothed profile. Positive velocities indicate flow moving away from the vessel negative velocities are moving towards the vessel.

From these profiles, the contributions of both the hull and propeller forcings can be better recognized. While the hull form creates strong hydrodynamics near the surface, the contributions of the propeller jet generate the highest velocities near the bed. As noted in Craig et al. (2023), these complex hydrodynamics are not captured by the analytical formula from Hamil (1987) and therefore may not accurately reflect the velocities in the propeller jet.

The maximum velocity produced at the lowest measured point of -13.8 m is 0.84 m/s. With this reference velocity, the bed shear stress can be found as 0.898 Pa using Nikuradse (1933) and Madsen et al. (1993). This exceeds the 0.67 Pa, critical shear stress of erosion for non-cohesive sediments, used in Tate et al. (2014) for the HSC. However, other values of critical shear stress can be determined. The channel bed contains a mix of fine sands, silts, and clays, USEPA/USACE (2016) found that the median grain size for the upper to lower bay sections of the channel falls between 0.042 to 0.111 mm. These sizes are representative of coarse silt to very fine sand where very fine sands have critical shear stresses of 0.11 to 0.145 Pa (USGS, 2013). With this, to maintain a conservative approach, comparisons will be conducted using the 0.67 Pa critical shear stress, but the exceedance of the critical shear may be much greater.

For another measurement in C2 HAMPSHIRE, a tanker vessel, passed through the survey area and was followed by PATI R MORGAN, a tug pushing a deep draft barge. The full velocity profile measurement is shown in Figure 26 with select profiles shown in Figure 27. In this case, the propeller wash from both vessels is mixed and the measurements capture the combined effects. Unlike profile 3 $x/D_\mathrm{p} = 250$ captured for UOG DESPINA V, in Figure 27 profile 1 for the combined wake at $x/D_\mathrm{p} = 230$ shows that while there is a weakened current towards the surface, the water column is moving away from both vessels. The pattern then flips from profiles 2 to 6 where there is flow moving towards the vessels at the lower half of the water column and moving away in the upper half. This may be a result of the PATI R MORGAN combination of the deep draft hull and shallow drafted propeller. While the propeller effects of these two vessels do not persist as far as those of the UOG DESPINA V, the bed shear loadings of the combined propeller wash are greater, reaching 1 Pa.

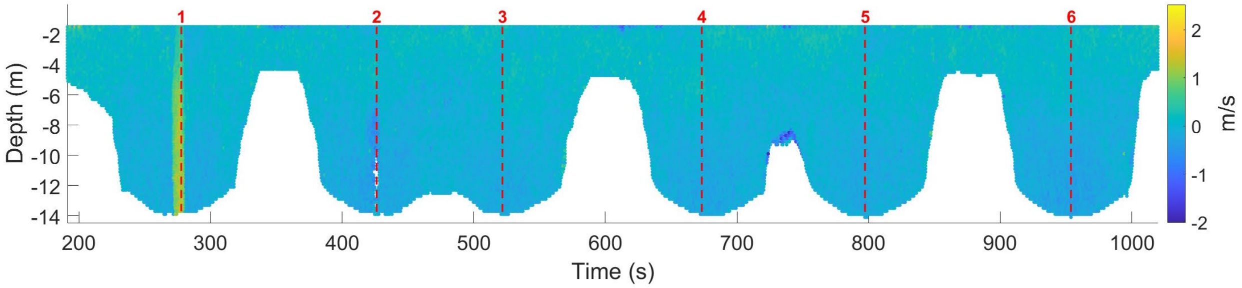

Figure 26. Measured velocity parallel with the channel produced by vessels HAMPSHIRE and PATI R MORGAN. Positive velocities (yellow) indicate flow moving away from the vessel negative velocities (blue) are moving towards the vessel.

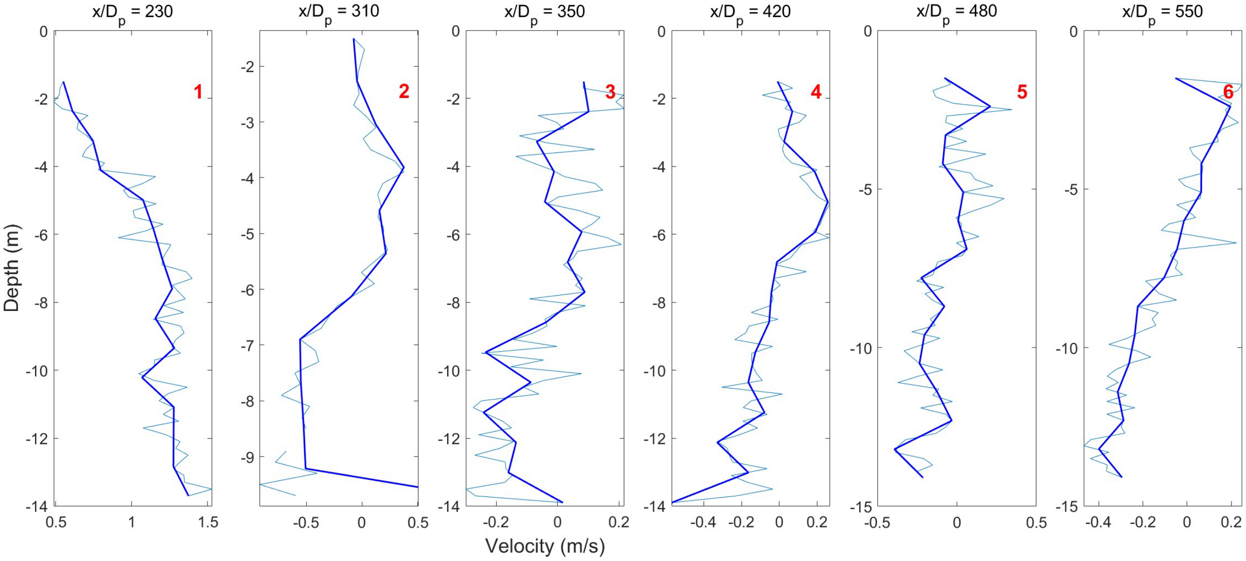

Figure 27. Select velocity profile transects produced by vessels HAMPSHIRE and PATI R MORGAN. Light blue line shows measured velocities while the dark blue line is the smoothed profile. Positive velocities indicate flow moving away from the vessel negative velocities are moving towards the vessel.

The vertical component of the measured velocity profiles is shown in Figure 28 for the vessel UOG DESPINA V as an example. Highlighted by the red box, upwards currents of up to 0.16 m/s coinciding with high velocities at the bed have the potential to suspend eroded sediments and distribute them throughout the water column. Visualized in the yellow box are indicated downwards velocities of 0.49 m/s. However, these may not represent real velocities as they coincide with low correlation ranging from 33 to 66 % and may be artifacts of acoustic interference near the bed. To get a better understanding of the upward velocities, it is necessary to analyze the vorticity.

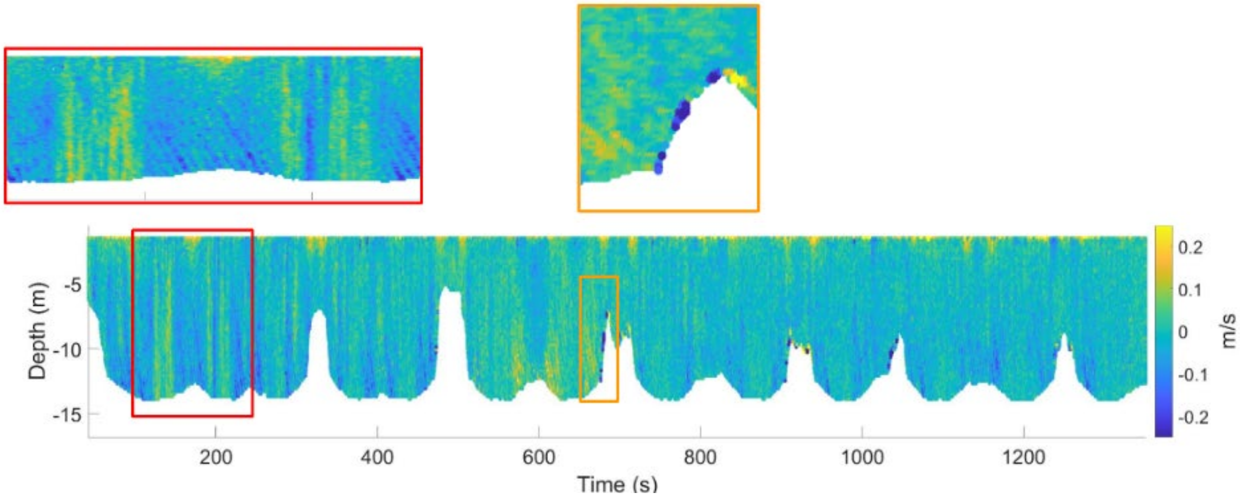

Figure 28. Measured vertical velocities produced by vessel UOG DESPINA V. Note the increased upward component near the center of the channel (red box inset) and increased downward component along the channel banks (yellow box inset).

By determining the vorticity, larger eddies and flow structures that may contribute to sediment resuspension and transportation can be identified. When analyzing the vorticity for propeller wash, dipole vortices can be picked out from the profiles. These vortices are shown in Figure 29 and Figure 30 for two different passing vessels, where positive vorticity indicates counterclockwise rotation and negative vorticity indicates clockwise rotation. The axis for the flows is again aligned with the propeller where the x-axis is along the axis of rotation, the y-axis is perpendicular to this aligned across the channel, and the z-axis is vertically aligned. For x-axis vorticity, there are multiple eddies formed near the middle of the water column in Figure 29, while in Figure 30 this structure is not present. This may be a result of the distance of the vessel from the measurement as the CGM MELISANDE was approximately 440 m away from the first transect, while the UOG DESPINA V was approximately 780 m away from the first transect. These x rotational vortices can contribute to lifting the sediment of the bed and distribute suspended sediments into the water column. For y-axis vorticity for both vessels, there appears to be no clear formations of eddies. The z-axis vortices for both the CGM MELISANDE and UOG DESPINA V show clear sets of dipole vortices throughout multiple transects. Where a set of dipoles can be identified by adjacent oppositely rotating flows. While the x-axis vorticity with the rotation of the propeller, z-axis rotations may correspond to the pressure field of the moving hull.

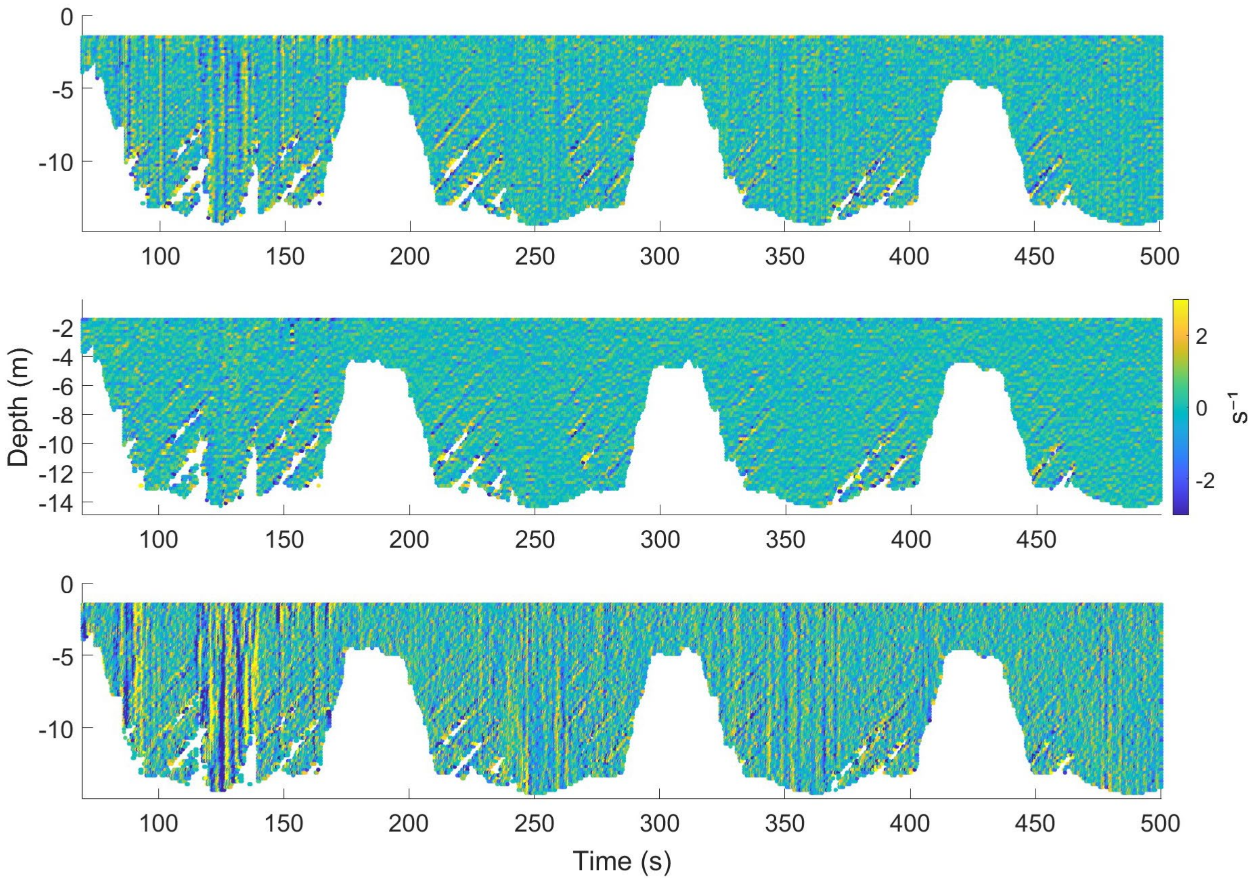

Figure 29. Measured x-vorticity (top), y-vorticity (center), z-vorticity (bottom) produced by vessel CMA CGM MELISANDE highlighting dipole vortices. Positive (yellow) vorticity indicates counterclockwise rotation, while negative (dark blue) vorticity indicates clockwise rotation.

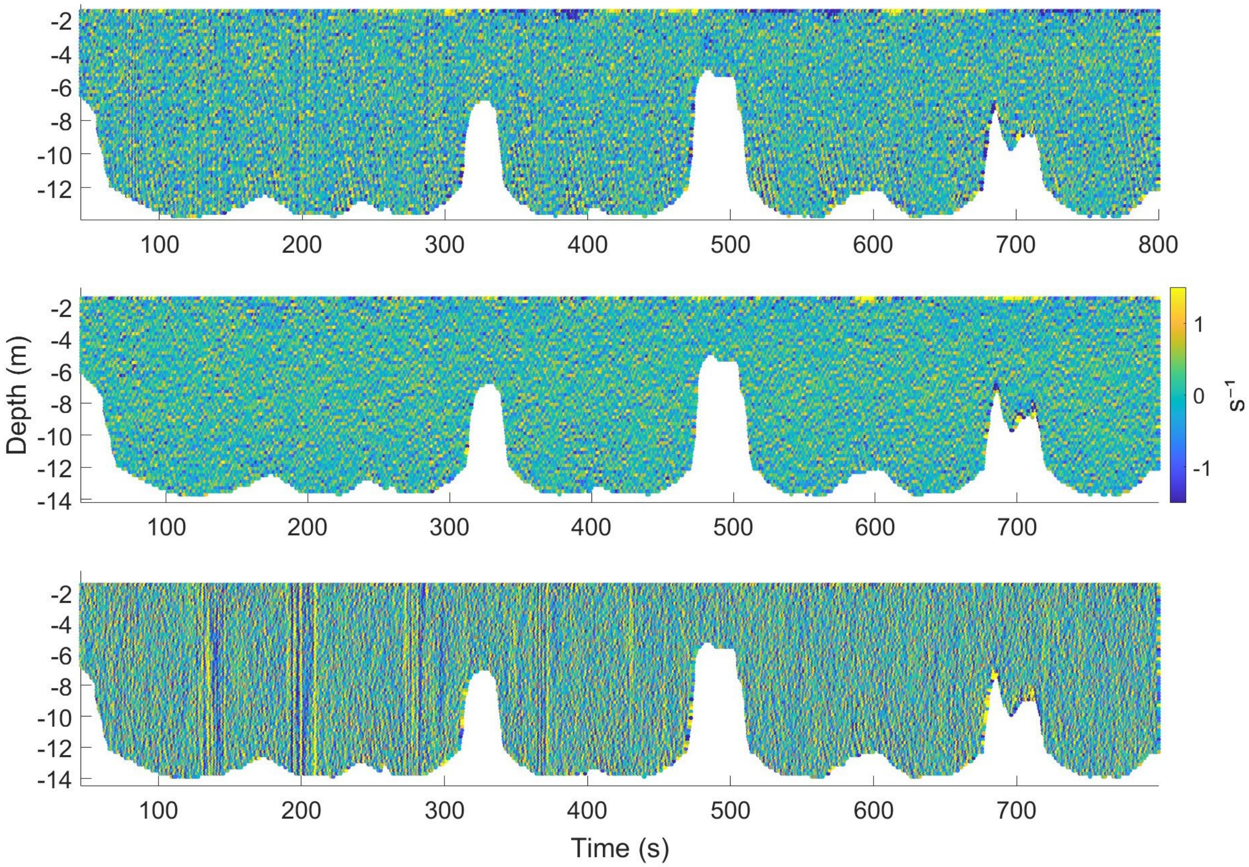

Figure 30. Measured x-vorticity (top), y-vorticity (center), z-vorticity (bottom) produced by vessel DESPINA V highlighting dipole vortices. Positive (yellow) vorticity indicates counterclockwise rotation, while negative (dark blue) vorticity indicates clockwise rotation.

Suspended Sediment Concentration (SSC) and Flux

With the application of the logarithmic relationship between known SSCs from collected water samples and measured backscatter, SSC is determined for each measured cell. The measured concentrations and sediment flux from each profile such for the tanker UOG DESPINA V shown in Figure 31 show the expectation of low background concentrations of 10.6 mg/L in non-impacted areas and higher concentrations of 840 mg/L in impacted segments. Deep draft vessels such as the CMA CGM MELISANDE with SSC and sediment flux shown in Figure 32 can create SSCs two orders of magnitude greater than background concentrations. For the DESPINA V measurement in Figure 31 it can be seen that the highest SSC of 840 mg/L is measured in the first channel cross-section. While this does coincide with the dipole vorticies captured in Figure 30, the current at this section is weak and dominantly moving twoards the vessel. With this while other vessels show the highest flux in the first cross-section, the highest flux for the DESPINA V does not occur until the second transect where it reaches up to 170 g/s. In contrast, the CGM MELISANDE had its highest sediment flux closest to the vessel reaching 360 g/s near the bed.

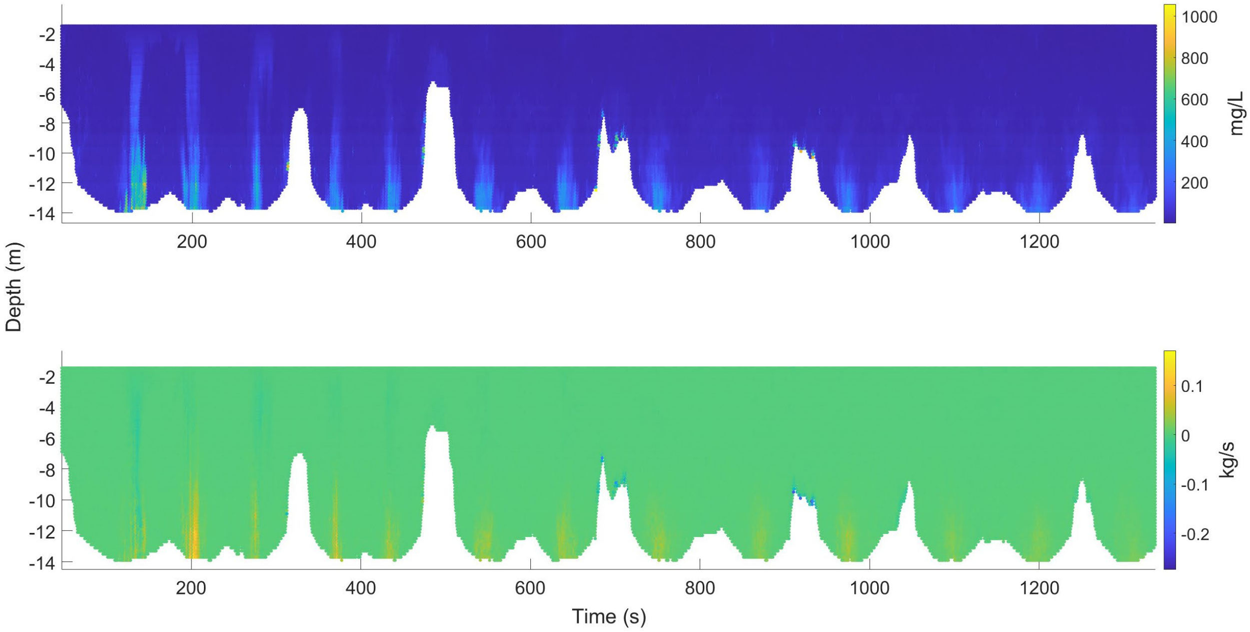

Figure 31. SSC (top) and suspended sediment flux (bottom) generated by vessel DESPINA V. Positive (yellow) flux indicates sediment moving away from the vessel, while negative (blue) flux indicates sediment moving towards the vessel.

Each vessel passing through navigational channels can not only resuspend sediments from the bed at the center of the channel near the location of the propeller but also introduce new sediment by lifting them into suspension along the slopes and the banks of the channel. When analyzing SSCs created by the CMA CGM MELISANDE shown in Figure 32, concentrations along the right side of the first channel crossing reach of up to 530 mg/L along the slope near the toe of the channel down to 80 mg/L near the top of the channel. The sediment flux of these particles reaches up to 100 mg/L which is comparable to those in the center of the channel for this same measurement. These concentrations may be a result of downward flow of water described previously (Figure 28) or other SSC mechanisms closer to the surface of the water could be related to the wake produced by the vessel hull (e.g., Tong et al. 2025).

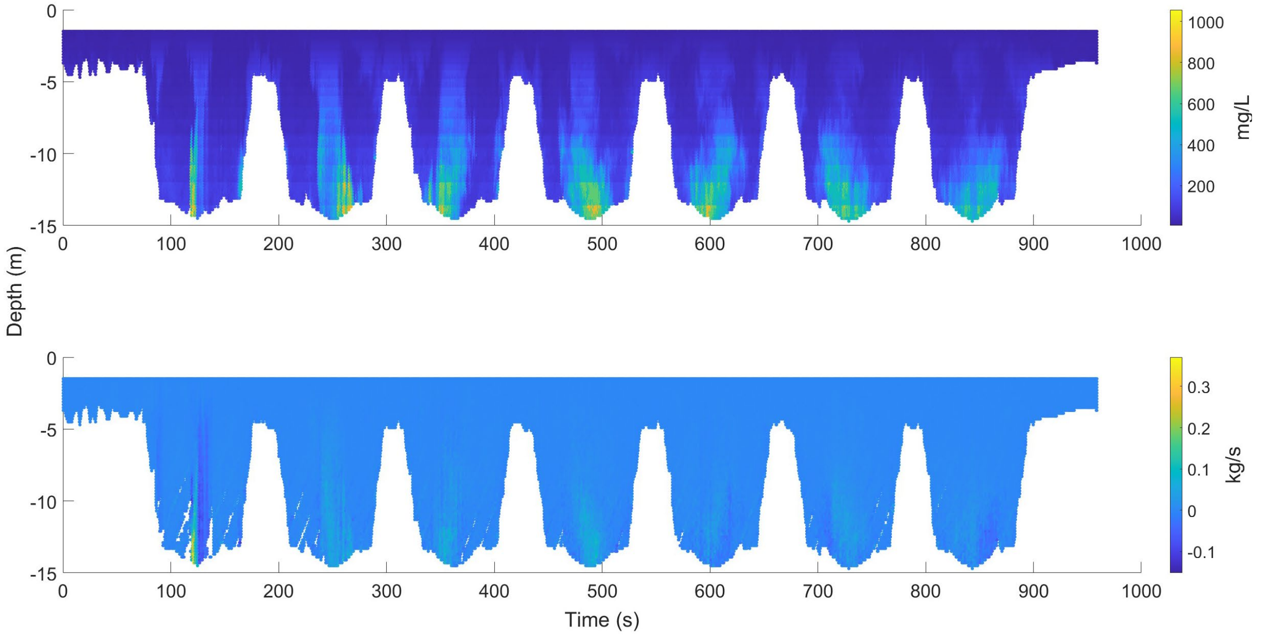

Figure 32. SSC (top) and suspended sediment flux (bottom) generated by vessel CMA CGM MELISANDE. Positive (yellow) flux indicates sediment moving away from the vessel, while negative (blue) flux indicates sediment moving towards the vessel.

While deep-draft vessels might suspend sediments along the slopes through secondary currents induced by propeller or wake hydrodynamics, tugboats passing through barge lanes or offset from the center of the channel also impact these areas. Though tugboats, and the barges that they are pushing, have relatively small drafts, they tend to travel along shallower slopes. As shown in Figure 33, though the sediment plume and flux from the deep draft vessel BRENTHOLMEN reaches up to 421 mg/L and 73 g/s respectively, the sediment suspended by the tugboats at the top of the channel directly impact the slopes. The leftmost plume captured at a time of 40 s is created by the tug MICHELLE ELISE which had a single barge configuration and suspended up to 105 mg/L near the bed but only has a sediment flux reaching 7 g/s. The rightmost plume between times of 120 and 140 seconds is caused by the tug Bud Sonier which had 2 barges in series. The plume generated by BUD SONIER has SSC that reaches 210 mg/L and sediment flux of up to 31 g/s. While the tugs have concentrations and sediment fluxes half or less than those induced by BRENTHOLMEN, these suspended sediments can be further transported and pulled into the channel by other passing vessels through their propeller wash and hull wake.

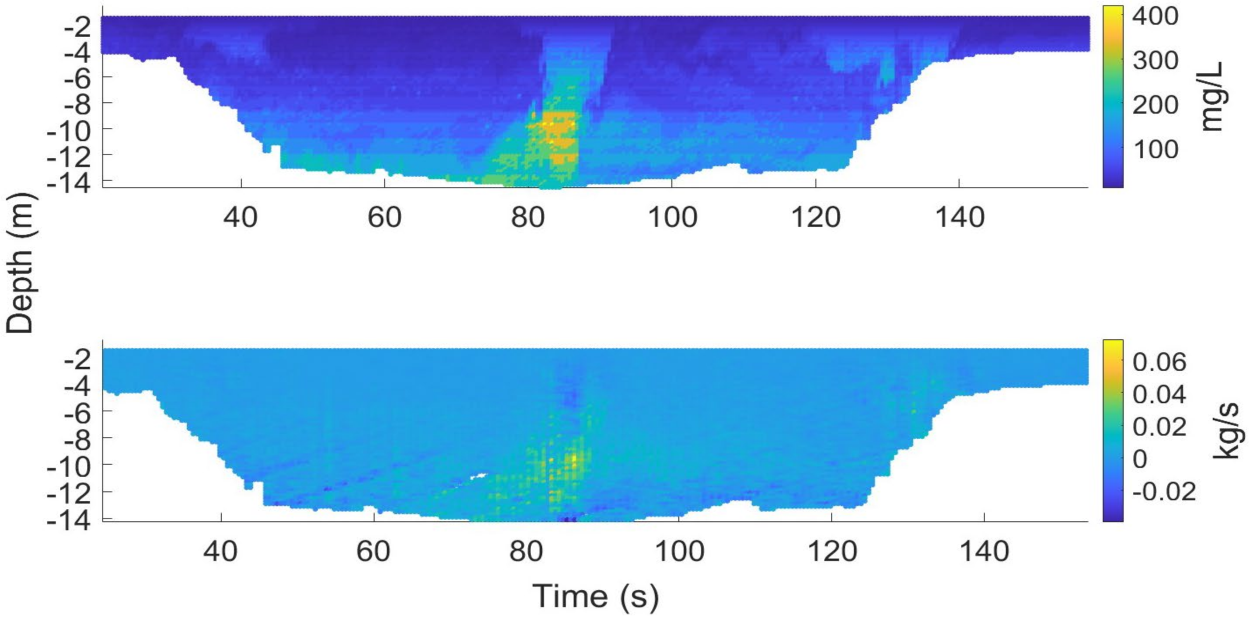

Figure 33. Comparison of SSC (top) and flux (bottom) produced by simultaneous passage of tugs BUD SONIER (top right of channel), MICHELLE ELISE (top left of channel), and deep-draft vessel BRENTHOLMEN (channel center).

A measurement containing primarily the impacts of a single tug is shown in Figure 34 for the GOOD SHEPHERD pushing two barges in series. While remnants of a previous vessel passing can be found near the center of the channel, the GOOD SHEPHERD impacts are shown on the left slope. The tug was able to produce SSCs of up to 210 mg/L near the bed and up to 6 m of water depth. Along with this, sediment fluxes up to 51 g/s were generated near the bed.

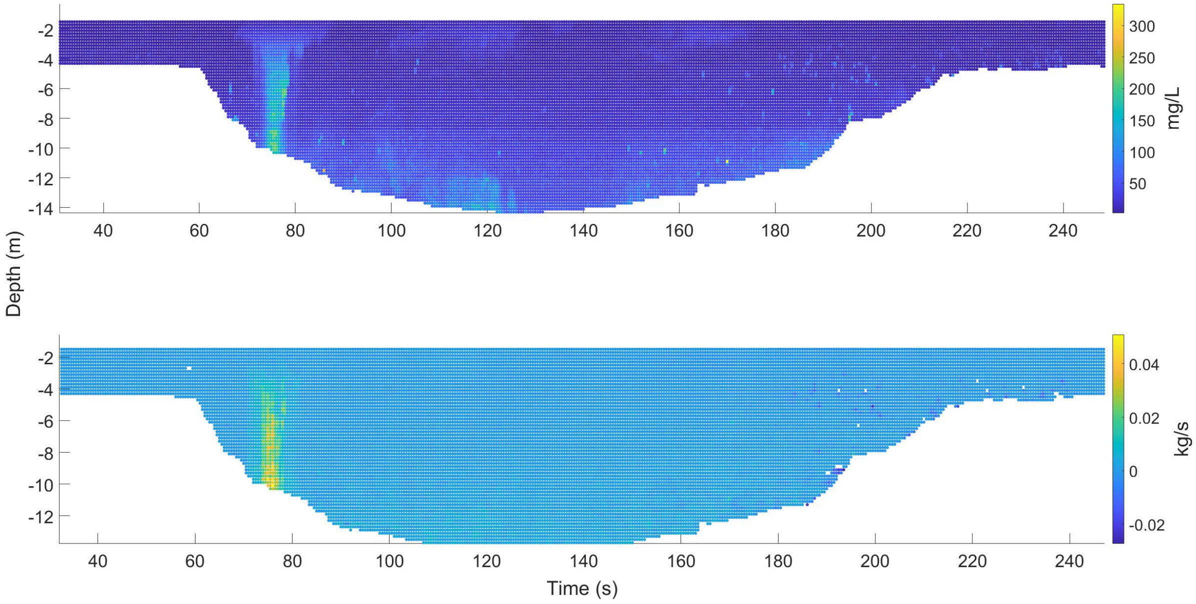

Figure 34. SSC (top) and suspended sediment flux (bottom) generated by vessel GOOD SHEPHERD. Positive (yellow) flux indicates sediment moving away from the vessel, while negative (blue) flux indicates sediment moving towards the vessel.

Electrical Resistivity

Figure 35 shows the electrical resistivity distributions of surveys S1 through S4, the remaining five surveys are included in Appendix B. It is important to note that the range of electrical resistivity values presented within Figure 35's color scales do not align with the true range of electrical resistivity; this was done to allow for direct visual comparison between sub-figures. These four surveys were selected as they best illustrate the effect of suspended sediments on water column electrical resistivity and align with data from ADCP measurements. Before comparing ADCP measurements with marine electrical resistivity measurements, the interpretation of the inverted electrical resistivity sections independent of the ADCP results are presented. In Figure 35a (S1) and Figure 35b (S2), the inverted electrical resistivity section of a survey without a vessel is compared to a survey which did follow a vessel. The depth of the survey is shown on the vertical axis, and the horizontal distance is displayed at the top. The solid black line in each sub-figure represents the channel floor for each survey section. In Figure 35a, there is a clear distinction between the more resistive channel floor (> 0.6 Ohm-m) and the less resistive water column (< 0.5 Ohm-m). At 759, 783, 806, 822, and 861 m, the inverted electrical resistivity section of Figure 35b shows multiple pockets of lowered electrical resistivity (0.1 Ohm-m). The channel floor in S2 is not as clearly defined compared to S1 due to smoothing effects from the pockets lowering the appearance of the channel floor. The RMS of S1 and S2 are 13.56% and 14.87%, respectively. Both inversions were able to converge in three iterations and reach an L2-Norm value at or near unity.

Figure 35c is survey S3 and Figure 35d is survey S4. Both S3 and S4 measured the water column resistivity behind a deep draft vessel, though S3 was conducted transverse to the HSC while S4 was conducted longitudinally. Like S1, S3 and S4 show a strong divide between the more resistive channel floor (> 0.6 Ohm-m) and less resistive water column (< 0.45 Ohm-m). S3 in Figure 35c shows fewer pockets of lowered electrical resistivity and the water column's appearance is smoother than S4's. For S3, the pocket with the smallest electrical resistivity value is located at 114,193 m and has a value of 0.3 Ohm-m. S4 has a large pocket of lowered electrical resistivity (0.2 Ohm-m) at a distance of 110,835 m. The RMS of S3 and S4 are 14.56% and 13.36%, respectively. The L2-Norm of both surveys are at unity. S3 converged in three iterations while S4 converged in 2.

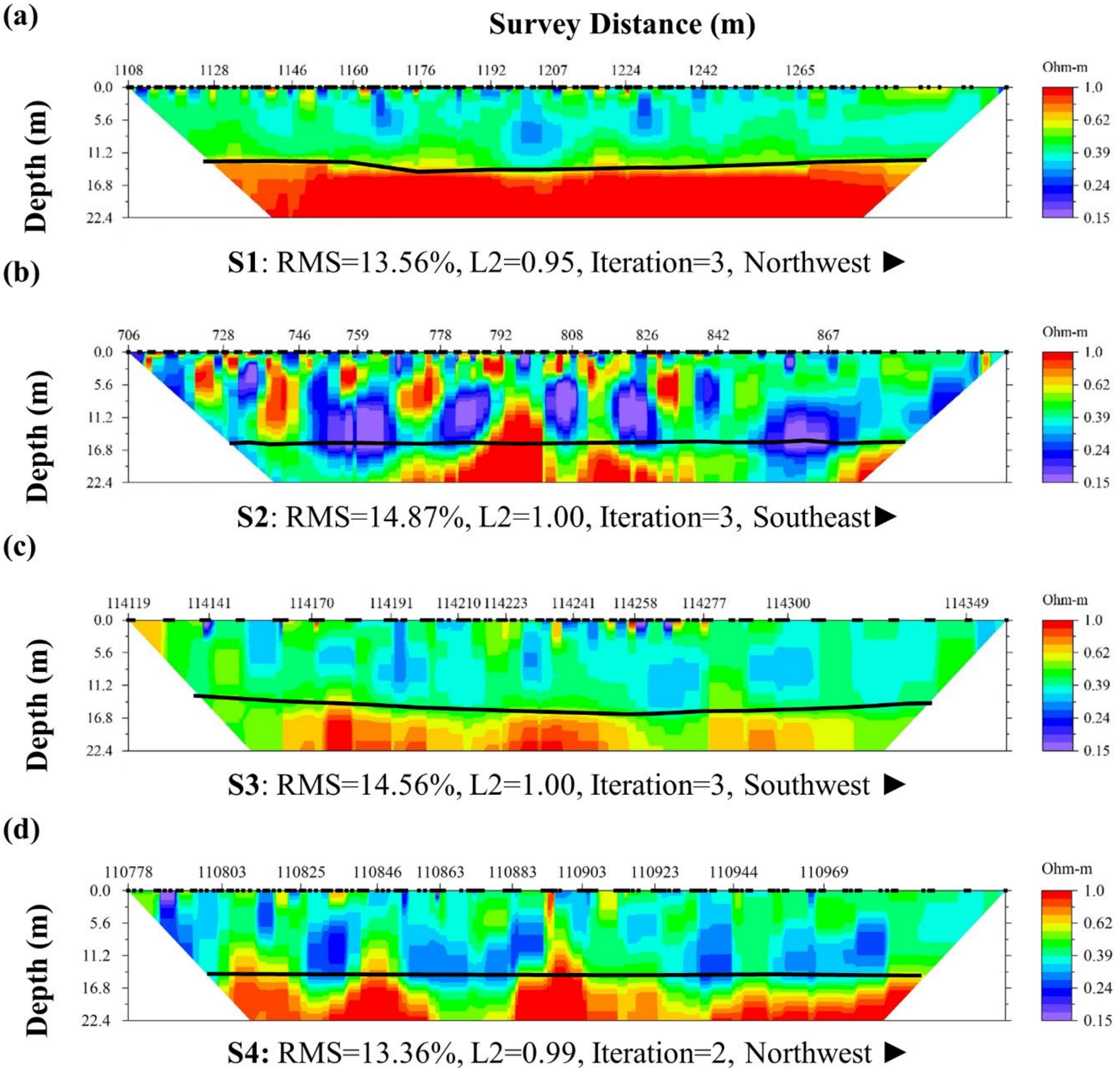

Figure 35. Electrical resistivity distribution of surveys S1 (a), S2 (b), S3 (c), and S4 (d). The distance of each survey is shown at the top in meters, and the depth in meters is provided on the left. The solid black line denotes the depth of the water for each respective survey.

Figure 36a shows the comparison of the average water column electrical resistivity with respect to depth for S1 and S2. Figure 36a shows that S2 has the smaller electrical resistivity in the water above the channel floor (9.5 m in depth to 12.7 m). Within this range, Figure 36b shows the maximum difference between S2 and S1 is 34.7%. Via the KS test, the water column resistivities for S1 and S2 are significantly different at the $p < 0.05$ level, D (23, 20) = 0.509, p = 0.005. Figure 36c shows the average water column electrical resistivities for S3 and S4. The electrical resistivity of both surveys is the same through the water column. Below the channel floor (15.3 m), the electrical resistivities start to diverge. This is further seen in Figure 36d, where the percent difference between S3 and S4 reaches a maximum of 6.38% at the water surface; from a depth of 2.5 m below the water surface to the channel floor, the maximum percent difference is 3.29%. From the vessel-vessel comparison, the two surveys are not significantly different at the $p < 0.05$ level, $D(18, 18) = 0.333$, $p = 0.275$.

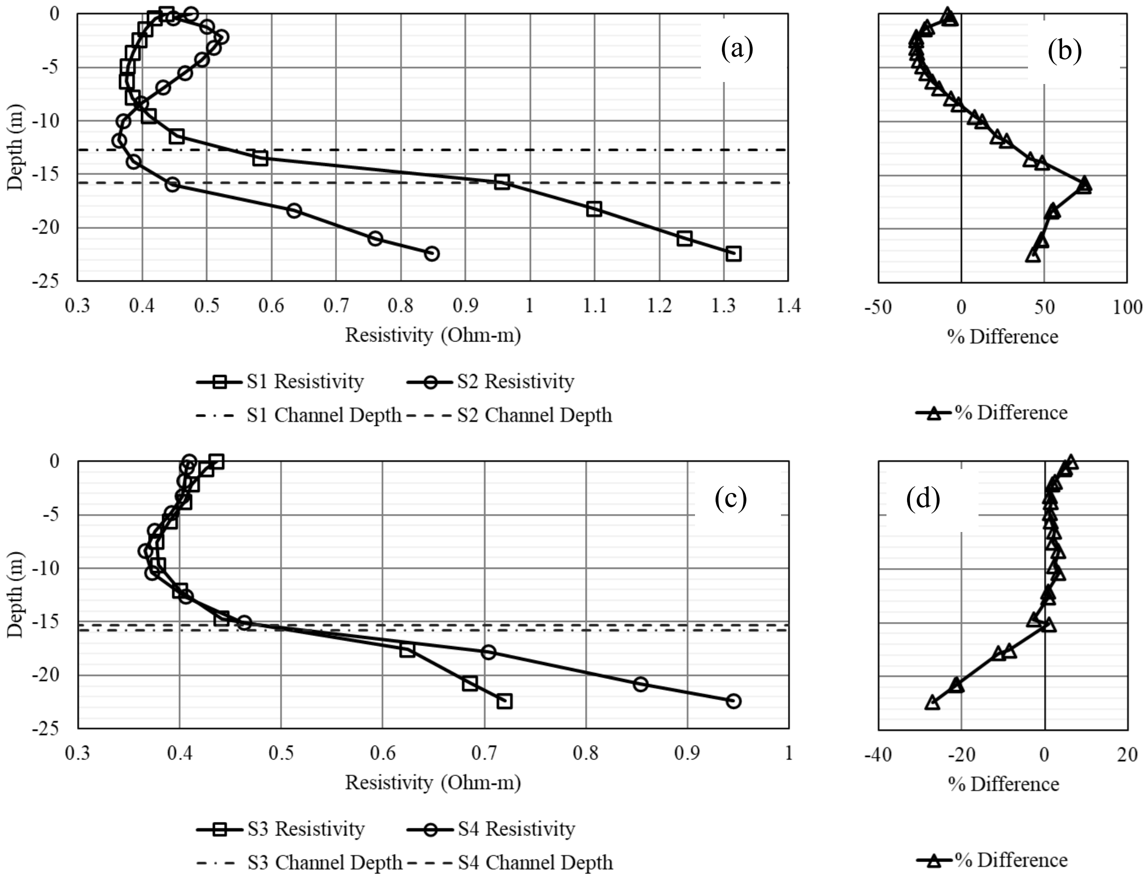

Figure 36. (a) Average water column electrical resistivity, with respect to depth, for S1 and S2; (b) Percent difference between the average water column electrical resistivity of S1 and S2; (c) Average water column electrical resistivity, with respect to depth, for S3 and S4; and (d) Percent difference between the average water column electrical resistivity of S3 and S4.

Interpretation of electrical resistivity results following a similar method to SSC interpretation is difficult. ADCP results in Figure 33 and Figure 34 show clear sediment plumes, while a clearly defined plume in the inverted electrical resistivity section of Figure 35 is not as apparent. Thus, the average electrical resistivity with depth was used to understand how sediments impact the water column electrical resistivity. Results from Figure 36a show that a decrease in electrical resistivity at the channel floor occurs when a vessel is present. Therefore, identifying when inverted electrical resistivity sections show a decrease in water column electrical resistivity at the channel floor and matching them with sediment plumes from ADCP measurements provides confidence that the two methods agree. Figure 37 shows the percent change from the NOAA reported water electrical resistivity and the measured electrical resistivity for S1, S2, S3, and S4. Figure 37 shows the water column electrical resistivity at the channel floor for S1 is 4.51% larger than the average water resistivity. Figure 37 also shows that for S2, S3, and S4, the water column electrical resistivity has changed -13.3%, 0.2%, and -6.8% from the background resistivity of 0.51 Ohm-m at the channel floor.

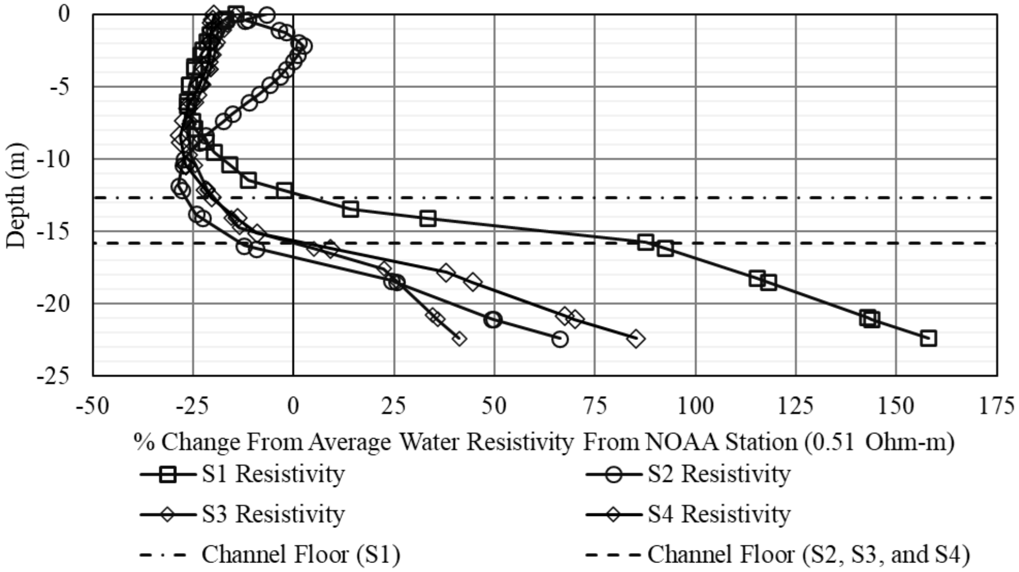

Figure 37. Percent change from NOAA reported water electrical resistivity (0.51 Ohm-m) for surveys S1, S2, S3, and S4.

S1 and S2 (Figure 35a and b, respectively) show that when a vessel is present, the electrical resistivity of the water column near the channel floor decreases. A difference of 34.7 % between S1 and S2 was found at the channel floor. This aligns with Hong et al. (2016) and Craig et al. (2023), where higher concentrations of suspended sediments are reported near the waterbody floor due to vessel propeller activity. These findings are also supported by the data shown in Appendix B, where four additional statistically significant survey comparisons identified at least a 15% difference in water column electrical resistivity at the floor of the HSC. Table 6 contains the additional comparisons. The magnitude of the difference in electrical resistivity is small; however, this aligns with work by Amidu and Dunbar (2008), where salinity changes caused a change of less than 0.6 Ohm-m in the water column. Compared to traditional land surveys, where differences in electrical resistivity are often on the scale of orders of magnitude (Loke, 2001), the suspended sediment does not change the electrical resistivity dramatically within the water column. The comparison of Surveys S3 and S4 shows that regardless of survey orientation, using marine electrical resistivity to measure sediment plumes will reveal a similar response. Furthermore, S3 and S4 were not found significantly different, as expected, because both were collected following a vessel. An additional TV-TV (transverse with vessel vs transverse with vessel) comparison also found a small percent difference (1.2%) at a non-significant p-value (0.081) further supporting the findings (see Table 6). The ability to measure the same response regardless of survey orientation is important as not all sites will have available survey space to the sides of a shipping channel. Around the HSC, Galveston Bay provides ample survey room, a luxury not afforded to all ports should others use similar methods to observe resuspended sediments. Additionally, the electrical resistivity at the channel floor for S1 through S4 was less than the electrical resistivity reported by NOAA on the day of C3 (0.51 Ohm-m), this indicates that water column electrical resistivity values within shipping lanes are lower than values outside shipping lanes. Thus, it is possible that propeller shear on the sides (as seen from tugboats) and on the bottom (generated from deep draft vessels) of shipping lanes resuspends sediments (Guarnieri et al. 2021). This resuspension of sediments from vessels traversing the HSC creates a measurable change in water electrical resistivity. As such, electrical resistivity serves as an indirect indicator of SSC for the water column.

Table 6. Survey comparisons supporting findings.

Surveys Compared	Comparison Type	% Difference	KS Test *P*-Value
S5 vs. S2	TNV v. TV	17.21	0.0001
S5 vs. S9	TNV v. TV	28.79	0.009
S6 vs. S1	TV v. PNV	18.25	0.006
S1 vs. S8	PNV v. TV	28.40	< .0001
S6 vs. S8	TV v. TV	1.20	0.081

Note: T=transverse the HSC; P=parallel (i.e., within) HSC; NV=no vessel; V=vessel

SSC and Electrical Resistivity

It has already been shown that measurements from the ADCP can image sediment plumes generated from deep draft vessels. Changes in water column electrical resistivity induced by resuspended sediments from deep draft vessels are measurable with marine electrical resistivity. Figure 38 shows the suspended sediment concentrations of the HSC for Surveys S3, S2, and S4. The ADCP was not measuring during Survey S1 so a comparison between the two is unavailable. The maximum concentration of S3's sediment plume is 420 mg/L (Figure 38a) and extends approximately 5 m above the channel floor. When compared to the measured electrical resistivity value in Figure 37 at the same depth, the water has an electrical resistivity of 0.37 Ohm-m, a 25% decrease from NOAA. Looking at the sediment plume from Survey S3, Figure 38b, the maximum concentration (666 mg/L) occurs at a survey time of 605 s, and the plume extends about 5 m off the HSC channel floor. The electrical resistivity for S2 is 27% less than 0.51 Ohm-m. Figure 38c shows the SSC for S4 as it followed behind a deep draft vessel in the HSC; as seen in the figure, SSC increases with depth. At the water surface, Figure 38c shows a concentration of 10 mg/L while the channel floor shows concentrations larger than 200 mg/L.

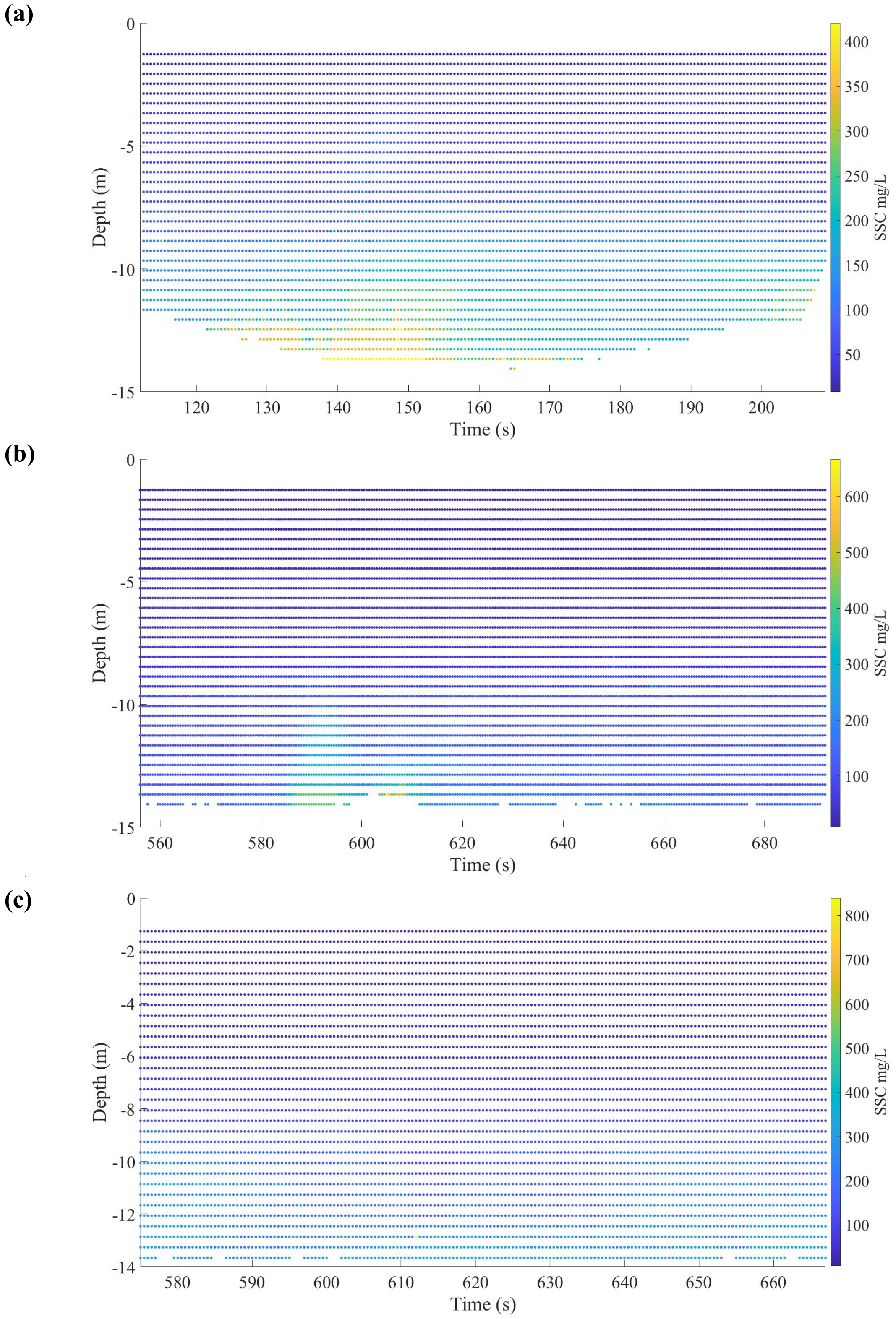

Figure 38. SSC During S3 (a), S2 (b), and S4 (c).

IMPLEMENTATION

The findings will be implemented in a future project with the Port of Houston to better estimate and predict channel dredging needs based on vessel traffic forecasts in the Houston Ship Channel among other parameters. Quantifications of suspended sediment concentrations related to vessel and transit characteristics will be incorporated into weighting functions for machine learning algorithms that are intended to help predict channel shoaling.

RECOMMENDATIONS AND CONCLUSIONS

Current velocities and backscatter amplitudes from vessel-mounted ADCP field measurements conducted over three separate campaigns in the Houston Ship Channel (HSC) in Galveston Bay, Texas, were used to derive estimated sediment concentrations, and flux values produced by deep draft vessel propeller wash. The rotating propeller(s) behind passing vessels can generate SSCs greater than 1,000 mg/L. These suspended sediments are then transported through the continuing propeller jet reaching sediment fluxes of up to 200 g/s. After the initial vessel passes, suspended sediments can be transported by ambient hydrodynamics or other passing vessels propeller wash and wake and settle into low energy zones. In addition, secondary flows of large deep draft vessels possibly due to their wake can generate SSCs of 530 mg/L along the slope near the toe of the channel. Tugboats traveling along the slope of the channel can have an equal impact on sedimentation despite being smaller than deep-draft vessels. Tugboats can regularly match SSCs of some deep draft vessels in the center of the channel producing SSC's up to 200 mg/L. While the fluxes of these tugs can only reach half of that of deep draft vessels, the SSC's remaining can be transported by other passing vessels or ambient hydrodynamics.

Electrical resistivity measurements taken concurrently with ADCP measurements were collected over a single-day field campaign. Comparisons of electrical resistivity values to determine the effectiveness of the method concluded that a towed marine electrical resistivity survey is able to detect bulk changes in water column electrical resistivity in seven surveys due to deep draft vessels. Statistical testing validates that the electrical resistivity distribution for vessel-non-vessel comparisons are significantly different. Similarly, comparing surveys with no vessel is present in either are significantly similar. Comparisons with ADCP data reveal that five electrical resistivity surveys show a decrease in electrical resistivity near the channel floor when a plume is present, and one survey shows no change in electrical resistivity when a vessel is not present. Some of the challenges faced with using marine electrical resistivity to image sediment resuspension stems from the inversion process. As discussed with Figure 35b, smoothing effects caused the appearance of the channel floor to be lower than its actual value. If reversed, it is possible that smoothing effects in the inversion process removed pockets of lowered electrical resistivity. Additionally, the width of the inverted survey domain fit within the deepest parts of the HSC and avoided processing data over the edges of the HSC. Thus, insights from the effects of tugboat propeller shear are not provided by marine electrical resistivity methods. However, the towed surveys support ADCP measurements through bulk electrical resistivity analysis at the channel floor, as a measurable decrease in electrical resistivity is detected for surveys where a vessel is present.

DATA AVAILABILITY STATEMENT

All velocity profile data collected via vessel-mounted ADCP surveys, CTD and electrical resistivity probe measurements that support the findings of this study are in the Zenodo Data Share repository with the identifier https://doi.org/10.5281/zenodo.18189391 (Figlus et al., 2025).

REFERENCES

Amidu, S., and Dunbar, J. (2008). An evaluation of the electrical-resistivity method for water-reservoir salinity studies. *Geophysics*, 73(4): G39–G49. https://doi.org/10.1190/1.2938994

Berger, V.W. and Zhou, Y. (2014). Kolmogorov–Smirnov test: Overview. In *Wiley StatsRef: Statistics Reference Online* (eds N. Balakrishnan, T. Colton, B. Everitt, W. Piegorsch, F. Ruggeri and J.L. Teugels). https://doi.org/10.1002/9781118445112.stat06558

Binley, A. (2015). Tools and techniques: Electrical methods. In *Treatise on Geophysics* (ed. G. Schubert), 11. Cambridge, MA, Elsevier Science, 233–259, doi:10.1016/B978-0-444-53802-4.00192-5.

Bureau of Ocean Energy Management (BOEM) and National Oceanic and Atmospheric Administration (NOAA). MarineCadastre.gov. ais-2024-01-30.csv.zst. Retrieved January 26th, 2025 from marinecadastre.gov/data.

Bureau of Ocean Energy Management (BOEM) and National Oceanic and Atmospheric Administration (NOAA). MarineCadastre.gov. ais-2024-08-08.csv.zst. Retrieved May 17th, 2025 from marinecadastre.gov/data.

Bureau of Ocean Energy Management (BOEM) and National Oceanic and Atmospheric Administration (NOAA). MarineCadastre.gov. ais-2025-05-14.csv.zst. Retrieved November 20th, 2025 from marinecadastre.gov/data.

Craig, P. M., Jung, J. Y., Mausolff, Z., Bastidas, L. A., Mathis, T, and Wang, P.-F. (2023). Modeling sediment resuspension and transport processes induced by propeller wash from ship traffic. *J. Hydraulic Eng.*, 149(5): 04023009. https://doi.org/10.1061/JHEND8.HYENG-13229

Edwards, L. S. (1977). A modified pseudosection for resistivity and IP. *Geophysics*, 42, 1020-1036. https://doi.org/10.1190/1.1440762.

Everett, M. E. (2013). Electrical resistivity method. In *Near-Surface Applied Geophysics* (pp. 70–103). Cambridge University Press.

Federal Highway Administration (FHWA). (2019). Advanced geotechnical methods in exploration (A-GaME).

Accessed July 30, 2024. https://www.fhwa.dot.gov/engineering/geotech/agame/

Figlus, J. and Song, Y.-K. (2020). Corpus Christi Ship Channel ADCP and CTD Survey. Final Report (December 2020) for U.S. Army Corps of Engineers – Galveston District, p. 66, Department of Ocean Engineering, Texas A&M University / Texas A&M Engineering Experiment Station, Galveston, TX.

Figlus, J., Lawrence, A. M., Kulesza, S., and Gombac, A. (2025). Field data on propeller wash induced dynamics in the Houston Ship Channel [Data set]. Zenodo. https://doi.org/10.5281/zenodo.18189391

Gadgil, A. A. (2021). *Sediment movement due to non-linear forcing generated by irregular waves, pressure gradients, and ships*. Ph.D. dissertation, Texas A&M University. https://hdl.handle.net/1969.1/195316

Gombac, A., Kulesza, S., and Almikati, A. (2025). Efficacy of marine electrical resistivity surveys to determine maximum scour depth and scour infill. *Transportation Research Record: Journal of the Transportation Research Board*, 2679(10). https://doi.org/10.1177/03611981251341346

Google Earth. (2025). *Satellite imagery of the Houston Ship Channel near Eagle Point in San Leon, Texas* [Satellite image]. Retrieved March 28, 2025, from https://earth.google.com/

Guarnieri, A., Saremi, S., Pedroncini, A., Jensen, J. H., Torretta, S., Vaccari, M., and Vincenzi, C. (2021). Effects of marine traffic on sediment erosion and accumulation in ports: A new model-based methodology, *Ocean Sci.,* 17: 411–430. https://doi.org/10.5194/os-17-411-2021

Hamill, G. A. (1987). *Characteristics of the screw wash of a maneuvring ship and the resulting bed scour*. Ph.D. Thesis, Dept. of Civil Engineering, Queen's Univ. of Belfast, Ireland.

Hong, J.-H., Chiew, Y.-M., Hsieh, S.-C., Cheng, N.-S., and Yeh, P.-H. (2016). Propeller jet–induced suspended-sediment concentration. *Journal of Hydraulic Engineering*, 142(4): 04015064. https://doi.org/10.1061/(ASCE)HY.1943-7900.0001103

Koehn, W., Tucker-Kulesza, S., and Steward, D. (2019). Conceptualizing groundwater surface-water interactions within the Ogallala Aquifer with electrical resistivity. *Journal of Environmental and Engineering Geophysics*, 24(2): 85-199. https://doi.org/10.2113/JEEG24.2.185

Konaté, A., Kaba, O., Zaheer, M., Conté, M., Diallo, M., Thiam, B., and Oularé, F. (2023). Use of electrical resistivity tomography (ERT) for detecting underground voids on electrical pylon installation sites: Case studies from Labé Prefecture, Republic of Guinea. In *Proc. 9th Int. Conf. on Civil Eng.,* Singapore, 327: 611–620. Springer. https://doi.org/10.1007/978-981-99-2532-2_51

Landers, M. N., Straub, T. D., Wood, M. S., and Domanski, M. M. (2016). *Sediment acoustic index method for computing continuous suspended-sediment concentrations*. Techniques and Methods, 3–C5. U.S. Geological Survey. https://pubs.usgs.gov/publication/tm3C5

Leon, F. D. (2023). It’s official – Project 11 dredging is underway.” *Port Houston*. https://porthouston.com/project-11-dredging-underway/

Loke, M. H. (2001). Tutorial: 2-D and 3-D electrical imaging surveys. (p. 187). https://web.gps.caltech.edu/classes/ge111/Docs/ResNotes_Loke.pdf

Madsen, O. S., Wright, L. D., Boon, J. D., and Chisholm, T. A. (1993). Wind stress, bed roughness and sediment suspension on the inner shelf during an extreme storm event. *Continental Shelf Research*, 13(11): 1303–1324.

National Oceanic and Atmospheric Administration. (2025). Tides and Currents Eagle Point, Galveston Bay, TX - Station ID: 8771013. NOAA Tides and Currents. https://tidesandcurrents.noaa.gov/stationhome.html?id=8771013

Nagel, J. R. (2012). Solving the generalized poisson equation using the finite-difference method (FDM). Department of Electrical and Computer Engineering, University of Utah. https://my.ece.utah.edu/~ece6340/LECTURES/Feb1/Nagel%202012%20-%20Solving%20the%20Generalized%20Poisson%20Equation%20using%20FDM.pdf

Nikuradse, J. (1933). Strömungsgesetze in rauhen Rohren. VDI Forschungsheft, 361.

Passaro, S. (2010). Marine electrical resistivity tomography for shipwreck detection in very shallow water: A case study from Agropoli (Salerno, southern Italy). *J. Archaeol. Sci.*, 37 (8): 1989–1998. https://doi.org/10.1016/j.jas.2010.03.004

Pearson, A. J., Rucker, D. F., Tsai, C.-H., Fuchs, E. H., and Carroll, K. C. (2022). Electrical resistivity monitoring of Lower Rio Grande River groundwater intermittency. *Journal of Hydrology*, *613*, 128325. https://doi.org/10.1016/j.jhydrol.2022.128325

Reed, C. W., Kraus, N. C., Lin, L., MacDonald, N. J., and Davies, M. H. (2008). Estimation of shoaling for proposed channel deepening in an estuary, Matagorda Ship Channel, Texas, USA. In *Coastal Engineering Proceedings 2008*, 2774–2785. https://doi.org/10.1142/9789814277426_0229

Rucker, D. and Noonan, G. (2013). Using marine resistivity to map geotechnical properties: A case study in support of dredging the Panama Canal." *Surf. Geophys.*, 11(6): 625–638. https://doi.org/10.3997/1873-0604.2012017

Swarzenski, P. W., Reich, C., Kroeger, K. D., and Baskaran, M. (2007). Multi-channel resistivity investigations of the freshwater-saltwater interface: A new tool to study an old problem. In *International Symposium: A New Focus on Groundwater - Seawater Interactions, 24th General Assembly of the International Association of Hydrological Sciences (IAHS-AISH),* Perugia, Italy. (pp. 100–106).

Tate, J., Gunkel, B., Rosati, J., Wood, E., Sanchez, A., Thomas, R., Ganesh, N., and Pratt, T. (2014). *Houston–Galveston Navigation Channel shoaling study* (ERDC/CHL TR-14-14). U.S. Army Engineer Research and Development Center, Coastal and Hydraulics Laboratory.

Tong, F., Figlus, J., Joubert, J., and Fuller, W. P. (2025). Field measurements and numerical simulations of deep-draft vessel-wake hydrodynamics in a shallow-bay system. *Journal of Waterway, Port, Coastal, and Ocean Engineering,* 151(3): 04025011. https://doi.org/10.1061/JWPED5.WWENG-2213

U. S. Environmental Protection Agency, Region 6, and U.S. Army Corps of Engineers, Galveston District. (2016). Galveston, Texas ocean dredged material disposal site: Site Management and Monitoring Plan (SMMP).

U. S. Geological Survey. (2013). *Simulation of flow, sediment transport, and sediment mobility of the lower Coeur d'Alene River, Idaho.* (Scientific Investigations Report 2008–5093). U.S. Department of the Interior. https://pubs.usgs.gov/sir/2008/5093/

Wiese T., Greenhalgh S., Zhou B., Greenhalgh M., and Marescot L. (2015). Resistivity inversion in 2-D anisotropic media: Numerical experiments. *Geophysical Journal International*, 201(1): 247–266. https://doi.org/10.1093/gji/ggv012

Zhou J., Revil, A., Karaoulis, M., Hale, D., Doetsch, J., and Cuttler, S. (2014). Image-guided inversion of electrical resistivity data. *Geophysical Journal International*, 197(1): 292–309. https://doi.org/10.1093/gji/ggu001

APPENDIX A – LAB PROCEDURE FOR DETERMINING SSC FROM WATER SAMPLES

APPENDIX B – ADDATIONAL ELECTRICAL RESISTIVITY SURVEYS

APPENDIX C – VESSEL INFORMATION PAGES

Note that all the information and files related to appendices A – C can be found in the Zenodo repository: https://doi.org/10.5281/zenodo.17795566 (Figlus et al., 2025).